NOVEL APPLICATIONS OF FLUORESCENT IMAGING

by

ADNAN MUSTAFIC

(Under the direction of Mark A. Haidekker)

ABSTRACT

Two novel methods of fluorescent imaging including molecular rotors and cotton bolls are presented here. Molecular rotors are a subgroup of fluorescent molecules with the ability to form twisted intramolecular charge transfer (TICT) complexes. They can be used for fluorescent imaging of flow patterns due to their unique property of viscosity sensitive quantum yield. Cotton bolls emit fluorescence when the chlorophyll on their exterior carpal wall is photoexcited. A pest complex of stink bugs infests cotton boll crops and causes damage. A non-invasive method to determine damage to cotton bolls by stink bugs is developed for possible field applications of preventative measurements to minimize damage.

INDEX WORDS: Fluorescent Imaging, Molecular Rotors, TICT, Cotton bolls, Stink bugs

NOVEL APPLICATIONS OF FLUORESCENT IMAGING

by

ADNAN MUSTAFIC

B.S. Biological Engineering, The University of Missouri, 2007
M.S. Biological Engineering, The University of Georgia, 2009

A Dissertation Submitted to the Graduate Faculty
of The University of Georgia in Partial Fulfillment
of the
Requirements for the Degree

DOCTOR OF PHILOSOPHY

ATHENS, GEORGIA

2012

©2012

Adnan Mustafic

All Rights Reserved

NOVEL APPLICATIONS OF FLUORESCENT IMAGING

by

ADNAN MUSTAFIC

Approved:	
Major Professor:	Mark A. Haidekker
Committee:	William S. Kisaalita Peter A. Kner

Electronic Version Approved:

Maureen Grasso
Dean of the Graduate School
The University of Georgia
December 2012

Acknowledgments

I would like to acknowledge Mark Haidekker for teaching me how to be an engineer, committee members William Kisaalita and Peter Kner for support and advice, Michael Toews for a steady supply of cotton bolls, and Erin Roberts for help with cotton bolls analysis.

Contents

List of Figures

List of Tables

List of Abbreviations and Symbols

S_0 - singlet ground state

S_1 - first singlet excited state

S_2 - second singlet excited state

T_1 - first triplet excited state

E - photon energy

h - Planck constant ($6.626\text{x}10^{-34}$ J·s)

$\hbar$ - reduced Planck constant ($1.055\text{x}10^{34}$ J·s)

c - speed of light in vacuum (299,792,458 $\frac{m}{s}$)

λ - Wavelength

τ - Fluorophore lifetime

Γ - Fluorophore emission

$k_n r$ - non-radiative decay rate

TICT - Twisted intramolecular charge transfer

LE- Localy excited

DCVJ = 9-(dicyanovinyl)-julolidine

CCVJ - 9-[(2-Cyano-2-hydroxy carbonyl)vinyl]julolidine

CCVJ-TEG - CCVJ-triethylene glycol ester

CPVDA - p-[(2-cyano-2-propanediol ester)vinyl]dimethylaniline

η - Viscosity

ϕ - Quantum yield

EG - ethylene glycol

LED - Light-emitting diode

Chapter 1

Introduction

1.1 Brief Review of the Principles of Fluorescence

Light emission from molecules in electronically excited states is called luminescence [1]. Luminescence is further subdivided into fluorescence and phosphorescence. Fluorescence transpires once molecules are excited by photon absorption to singlet excited (S_1) states, where they are joined by an electron from the ground (S_0) state as shown in Figure 1.1. Subsequently, molecules return to the ground state while emitting photons. Energy of a photon can be described with:

$$E = \frac{hc}{\lambda} \tag{1.1}$$

where h is the Planck constant ($6.626 \text{x} 10^{-34}$ J·s), c is the speed of light in vacuum (299,792,458 $\frac{m}{s}$), and λ is the wavelength. For fluorophores, transitions from $\pi \rightarrow \pi^*$ systems ensue in wavelength ranges from 300 to 700nm. For a typical fluorophore perylene, transitions between singlet electronic states take approximately 10^{-15} s, and energy levels are typically 1500 cm^{-1} apart [1]. The average time a fluorophore spends between its excitation and return to the ground state is called lifetime, and is typically on the order of pico- to nanoseconds.

Fluorescence lifetime is defined as:

$$\tau = \frac{1}{\Gamma + k_{nr}} \tag{1.2}$$

where Γ is the fluorescent emission rate, and k$_{nr}$ is the non-radiative decay rate. The number of emitted photons with respect to the number of absorbed photons defines quantum yield ϕ:

$$\phi = \frac{\Gamma}{\Gamma + k_{nr}} \tag{1.3}$$

and in systems without non-radiative processes $\phi \longrightarrow 1$. Fluorophores like Lucifer Yellow and fluoroscein exhibit no microenvironment sensitivity, and typically have high quantum yields.

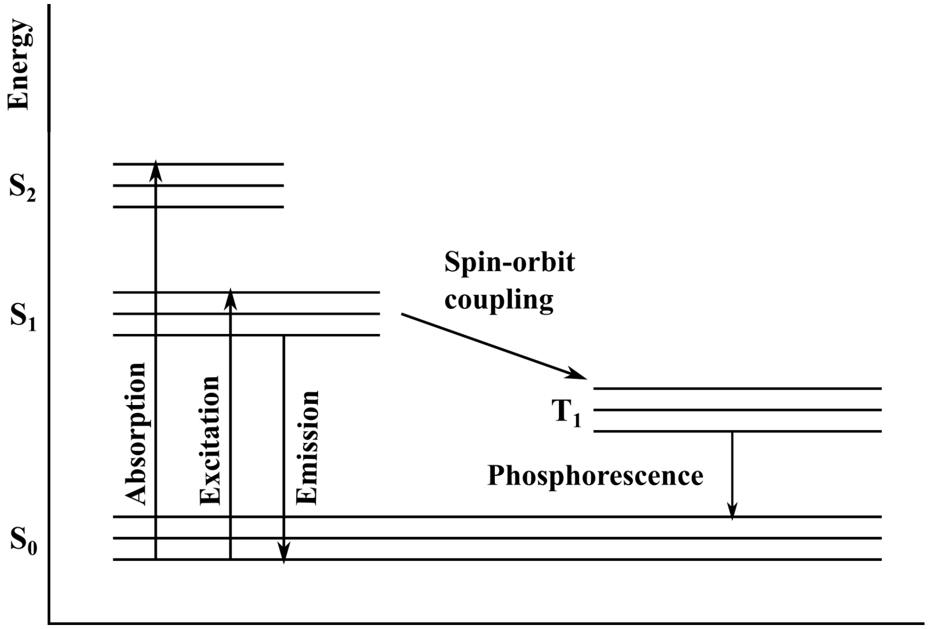

Figure 1.1: Jablonski diagram describing the process of absorption, fluorescence, and phosphorescence of a molecule with respect to its energy states. S$_0$ - singlet ground state, S$_1$ - first singlet excited state, S$_2$ - second singlet excited state, T$_1$ -first triplet excited state. Adapted from [1].

Emission of light from the first triplet excited (T$_1$) state is called phosphorescence. Phosphorescence takes place when molecules are excited to the S$_1$ state, where they may undergo a spin orbit coupling, where the spin orientation of electrons from the ground S$_0$ state and excited S$_1$ have their orbitals synchronized with regards to its spin orientation.

The position of an electron in an excited and ground state is approximated with Schrodinger's wave equation which determines the position of electrons in orbitals with different energy levels by calculating their respective probability densities:

$$i\hbar\frac{\delta}{\delta t}\Psi = \hat{H}\Psi \tag{1.4}$$

where Ψ is the wave function which describes the quantum state of an electron, i is the imaginary number, $\hbar$ is the reduced Planck constant, and $\hat{H}$ is the Hamiltonian operator denoting the total energy of a system. The reduced Planck constant is defined as:

$$\hbar = \frac{\lambda p}{2\pi} = \frac{h}{2\pi} = 1.055x10^{34} J \cdot s \tag{1.5}$$

where λ represents de Broglie's wavelength, p is the linear momentum of a particle, and h is the Planck constant.

Absorbed photons that lead to the excited state have higher energy than emitted photons, which according to the Franck-Condon principle, do not undergo nuclei displacement, and are most likely to emit from singlet excited state S$_1$ [1]. Their respective wavelength and position in vibrational states can be calculated with equations 1.1 and 1.4, and emission from distinct singlet excited states is represented with fluorescence emission spectra.

Fluorescence quantum yield can be influenced by several processes, namely quenching, photobleaching and temperature-dependent relaxation. Quenching reduces the quantum yield, and a typical case occurs when molecules like oxygen and halogens come into contact with fluorophores in excited states. Those molecules are called quenchers, and the reasons for this type of behavior has been postulated to be the cause of spin-orbit coupling and phosphorescence. The associated reduced fluorescence quantum yield is described with:

$$\frac{\phi_0}{\phi} = 1 + K[Q] = 1 + k_q \tau_0 [Q] \tag{1.6}$$

where K is the Stern-Volmer quenching constant, k_q is the bimolecular quenching constant, τ_0 is the unquenched lifetime, and [Q] is the quencher concentration [1].

Photobleaching is the process when the excitation light decreases the fluorophore emission potency, primarily because it brings about bond rearrangement and chemical destruction of the fluorophore in question. Intramolecular interactions between fluorescent molecules and their surrounding microenvironment dictates their degrees of freedom and hence the vibrational relaxation. High solvent temperatures increase the solvent relaxation rate by transferring energy to the fluorophores, thus changing their fluorescent quantum yield [9].

1.2 Fluorescence Spectroscopy

Fluorescence spectroscopy is used to detect and analyze fluorescence from biological and chemical samples with high sensitivity, and provides information about their respective processes [1]. It is especially popular in the analysis of biological samples due to its ability to non-destructively measure their physiological properties. Fluorescence is measured with a fluorometer, whose simplified schematic is shown in Figure 1.2. Excitation light is provided by an arc lamp (typically Xenon (Xe) or Mercury-Xenon (Hg-Xe)), which has a relatively high intensity, and it passes through a monochromator. Monochromators are gratings tasked with spatially separating collimated light into preselected wavelength ranges by diffraction, before they reach the sample.

The diffracted light then passes through the sample, followed by emission light passing through another monochromator to separate it from scattered excitation light. The average

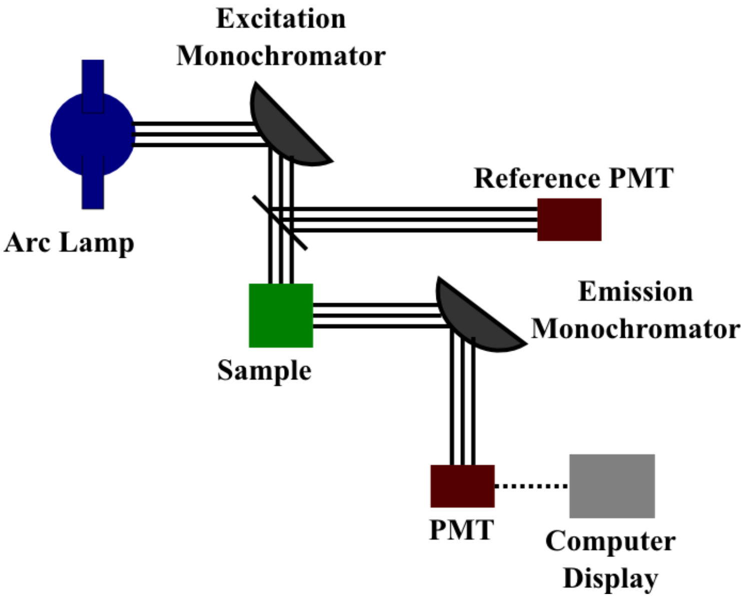

Figure 1.2: An L-geometry fluorometer schematic. Excitation light provided by an arc lamp is diffracted through a monochromator before it reaches the sample. Emission light is diffracted through another monochromator before it is detected by photomultiplier tube (PMT), and displayed on computer screen.

number of photons integrated over collection time is detected with a photomultiplier tube (PMT), and displayed. Typically, fluorometers are based on the L-geometry, where the excitation and emission light are measured at the right angle with respect to each other, and this setup has the advantage of spatially separating the excitation light from any contact with emission light detector. Fluorescence intensity tends to be proportional to the fluorophore concentration only when the optical density of the sample is greater than 0.1, and this is important since the phenomena of inner filter effect can reduce the quantum yield.

An excitation and emission graph of a 10 μM solution of CCVJ in ethylene glycol is shown in Figure 1.3. Energy losses in the vibrational modes makes the emitted light wavelength longer than the absorbed excitation light. The wavelength shift between the absorption maximum and emission maximum is defined as the Stoke's shift, and for CCVJ in ethylene glycol is 64 nm (exc=422nm, em=486 nm).

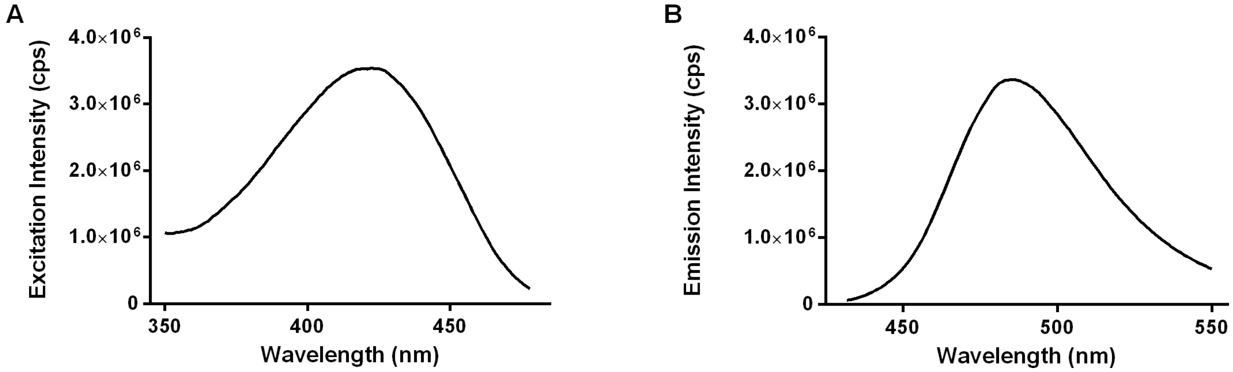

Figure 1.3: Excitation intensity (A) and emission intensity (B) graph of a 10 μM solution of CCVJ in ethylene glycol. Excitation peaks at 422 nm, while emission peaks at 486 nm. Stoke's shift is 64 nm.

1.3 Fluorescent Imaging Setup

A schematic for a simple fluorescence detection setup is shown in Figure 1.4. It consists of a narrow-band light source (arc lamp, LED, laser) providing excitation light which then passes through a collimator. Collimated light then passes through an excitation filter in order to select the wavelength frequency range needed to excite the sample. The sample absorbs the received light, thus inducing it to emit fluorescence. Emitted fluorescence needs to pass through a collimator to realign the light beam before before it reaches an emission filter which further restricts the emission wavelength and separates it from any scattered excitation photons. The resulting spectra detected by the photodetector can then be displayed and processed for additional analysis. A variation of the arrangement in Figure 1.4 to obtain spatially resolved fluorescence is shown in Figure 1.5. A large area of the sample is illuminated, and an objective creates a spatial relationship between local emission from the sample I(x,y) and the imaging plane.

Extended version of the aforementioned fluorescence setup was used in our experiments. Light source consisted of two LED's controlled with a custom driver with the ability to provide a continuous and homogeneous light. The overlap between emission and excitation spectra was reduced by placing 2 additional excitation filters in front of the LED's. Photodetection and image recording was done with an SLR camera which had an emission longpass filter in front of it. Modern cameras are built either with charged coupled devices (CCDs) or complementary metal-oxide semiconductor (CMOS) light sensor chips. Both types of light sensors have its advantages and disadvantages. In CCDs, light travels to the photoactive domain consisting of capacitors. The photon charges are converted into voltage and the values recorded digitally. CMOS light sensors contain a large number of MOSFET transistors responsible for logical operations. Due to the relative complexity of its design, photons traveling to its photodiode can miss its target. In this instance, our camera had a CCD chip.

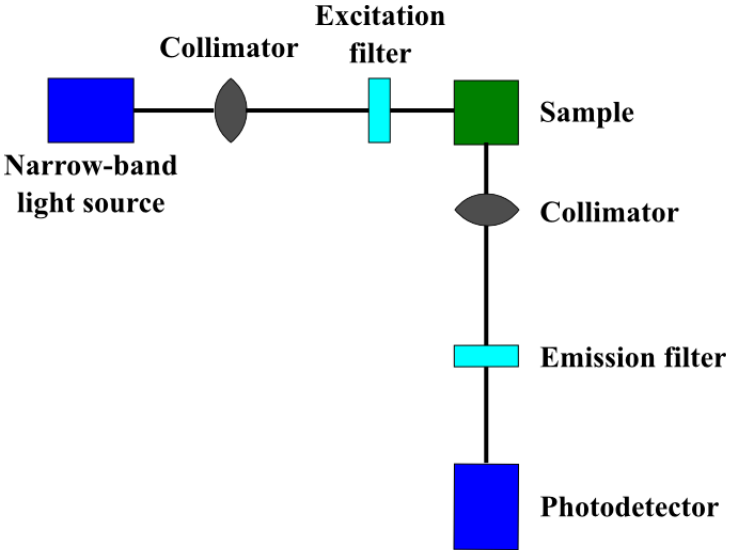

Figure 1.4: The simplest setup for fluorescence detection involves a narrow band light source, such as laser or LED, collimators to focus the beam, an excitation and and emission filter, and a photodetector for light sensing.

A schematic of a basic apparatus used to measure spatially resolved fluorescence typically used in fluorescent imaging and fluorescence microscopy, is shown in Figure 1.6 . In our case,

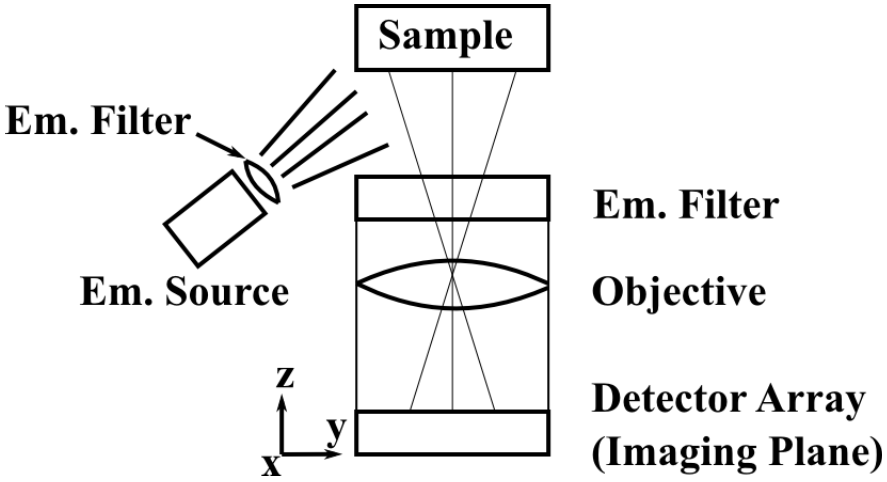

Figure 1.5: Variation of the arrangement in Figure 1.4 to obtain spatially resolved fluorescence. A large area of the sample is illuminated, and an objective creates a spatial relationship between local emission from the sample I(x,y) and the imaging plane.

light sources consisted of two blue LED's. The light passed through an excitation filter and lens system to narrow down the wavelength band so it is more suitable for sample excitation. Fluorescence emitted by the sample passes through a dichroic mirror before it reaches a CMOS (or CCD) chip, which can then process the signal with high spatial and temporal resolution.

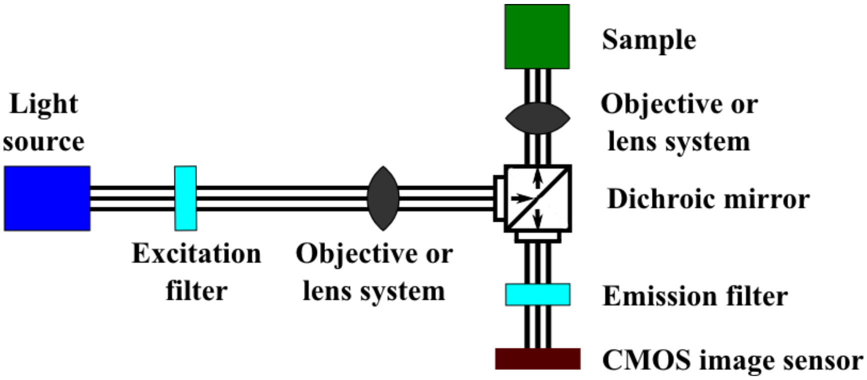

Figure 1.6: Schematice of a basic apparatus to measure spatially-resolved fluorescence (fluorescent imaging or fluorescent microscopy).

Measurements of various chemical reactions and molecular beam diagnostics have been successfully utilized with Laser-Induced Fluorescence (LIF) [10].Due to their aptitude to release large numbers of photons within a limited wavelength band, lasers can be used to excite target molecules within a sample, and measure their released emission with high efficiency. A different type of photodetectors constructed from silicon diodes has been in use for a long time [11]. They have been particularly popular in the field of radiometry because of their superior predictability and temporal stability.

Chapter 2

Molecular Rotors

2.1 Introduction

Fluorescent molecules form intramolecular charge transfer (ICT) complexes following charge separation from the electron donor to the electron acceptor group. Relexation to the ground state is followed by a red shift, and this effect is dependent on solvent polarity. Under electrostatic forces, a subset of fluorescent molecules has the ability to undergo a transition from ICT to TICT (twisted intramolecular charge transfer) complexes, and they are called molecular rotors. Once photoexcitation stops, they return from an excited state to the ground state either through fluoresnce emission or non-radiative molecular rotation [12]. This effect depends on the solvent viscosity, and in highly viscous solutions, fluorescence emission predominates, while in solutions with low viscosity, intramolecular rotation is the predominant pathway.

Molecular rotors posses and electron donor group connected to an electron acceptor group with a π conjugation spacer unit consisting of electron rich single and double bonds. The spacer unit plays an important role during intramolecular rotation around covalent σ bonds when it aids the movement of electrons from the donor to the acceptor group.

The formation of TICT complexes in in polar solvents was initially reported with p-N,N-dimethylaminobenzonitrile (DMABN), shown in Figure 2.1 [13]. The phenomenon was not observed in non-polar solvents, while the reported regular fluorescence emission was accompanied by an additional red-shifted emission with higher intensity. Later reportings showed the DMABN peak excitation to be 290 nm, and the two emission peaks at 342 and 460 nm [2].

Initial explanations regarding the formation of excimers and and locally emitting states were refuted by Rotkiewicz et al., who coined the TICT term, and suggested that the main reason for the TICT state inception rests with photoexcited fluorescent molecules in polar solvents, whose fluorescence emission increases with an increasing solvent viscosity, thus proposing a correlation between the two [14].

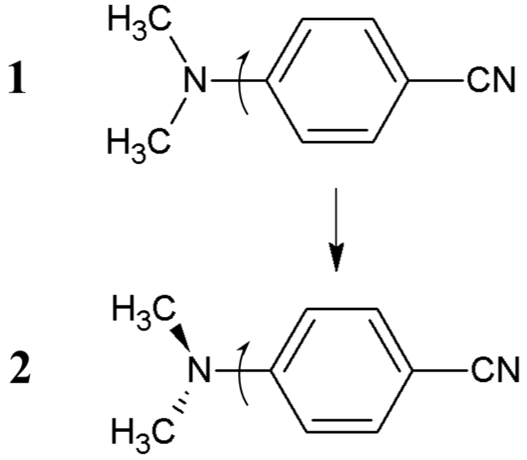

Figure 2.1: Chemical structure of p-N,N-dimethylaminobenzonitrile (DMABN). Arrows denote the bond of rotation from the locally excited state (1) to the TICT state (2). Rotationary angle θ=0 for the LE configuration, and θ=90 ° for the TICT configuration. Peak emission from the LE state is at 342 nm, and from the TICT state 460 nm [2].

A concomitant theory proposed that in the case of DMABN, twisting occurs when the dimethylamino group rotates around the single bond connecting it to the benzonitrile group, and ensues either from the locally excited (LE) state or the twisted TICT complex. Deexcitation from each state has different deexcitation energies, and the energy gap is $\approx$ 30 % lower in the TICT state when compared to the LE state energy gap, and it leads to a wavelength shift [4]. When the TICT energy gap between the S_1 and S_0 state is very low, relaxation does not result in visible and IR light emission, rather a single-emission band and solvent dependent quantum yield can be observed.

The dynamics of TICT complexes is dictated by the properties of its environment, most importantly solvent polarity. In highly viscous solvents, the rate of TICT formation is reduced due to sterical hindrance, while in highly polar solvents the rate of TICT formation is intensified due to increased hydrogen bonding [12].

Return to the ground state via intermolecular rotation is accompanied with energy loss and leads to a solvatochromic shift. The quantum yield ratio of the TICT (ϕ_{TICT}) and of the locally excited LE state (ϕ_{LE}) can be quantified in terms of their respective forward (k_a) and backward (k_d) reaction rates, and a schematic of the TICT potential energy surface is shown in Figure 2.2:

$$\frac{\phi_{TICT}}{\phi_{LE}} = \frac{k'_f}{k_f} \cdot \frac{k_a}{k'_f + k'_{nf} + k_d} \tag{2.1}$$

where k_f and k_{nf} are the radiative fluorescence decay rate and the non-radiative fluorescence decay rate for the LE excited state, respectively. k'_f and k'_{nf} are the radiative fluorescence decay rate and the non-radiative fluorescence decay rate of the TICT state, respectively [15].

When TICT state formation is dominant, $k_a \gg k_d$ and $k_d \ll k_f + k_{nf}$, Equation (2.1) can be rewritten as:

$$\frac{\phi_{TICT}}{\phi_{LE}} = Ck_a \tag{2.2}$$

where the dye specific constant $C=\frac{k'_f}{k_f(k'_f+k'_{nf})}$.

The solvent polarity affects the magnitude of the dipole moment, which in turn alters the system entropy. Increased system entropy increases the relaxation rate with which an excited molecule returns to the ground state, and the dielectric constant ϵ can be described

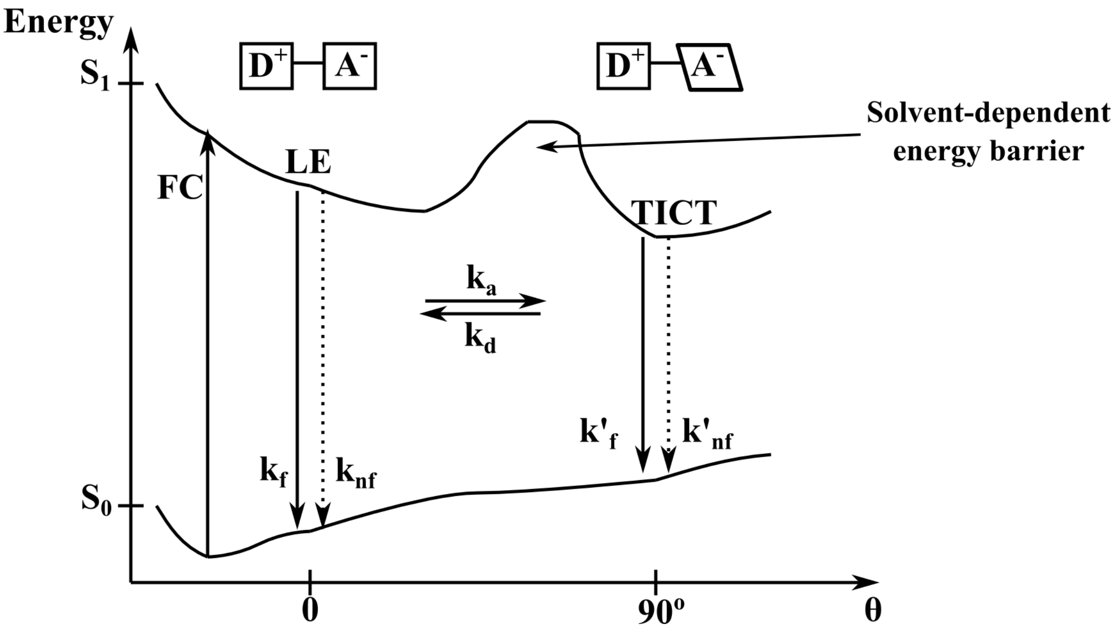

Figure 2.2: Potential energy surface of a fluorophore. Following excitation from ground state S_0 to singlet excited state S_1, fluorophore deexcites from a locally excited (LE) state to the lower energy TICT state while rotationary segment is rotated 90°. Solvent polarity and viscosity can present an energy barrier that reduces TICT formation rate. Singlet excited state state S_1, ground state S_0, locally excited (LE), Franck-Condon state (FC), rotationary segment angle θ. Adapted from [3, 4]

with:

$$\overline{V_a} - \overline{V_f} = \frac{2}{hc}\left(\frac{\epsilon - 1}{2\epsilon - 1} - \frac{n^2 - 1}{2n^2 + 1}\right)\frac{\mu_e - \mu_o}{a^3} \tag{2.3}$$

where $\overline{V_a}$ is the absorption wavenumber(or wave spatial frequency), $\overline{V_f}$ is the peak fluorescence emission wavenumber, h is the Planck consant, c is the speed of light, ϵ is dielectric constant, n is the refractive index, μ_e is the excited state dipole moment, μ_o is the ground state dipole moment, and a is the radius of volume occupied by fluorophores [16].

2.2 Förster-Hoffmann Equation

The relationship between the microviscosity of solvent and molecular rotors has been first described by Förster nad Hoffmann in 1971, who examined several triphenylmethylene (TPM) dyes, among the crystal dye shown in Figure 2.3 [3]. In their experiments they discovered that if solvent's viscosity increases, so the the quantum yield. This was attributed to intramolecular rotation of the 3 phenyl groups found in TPM dyes.

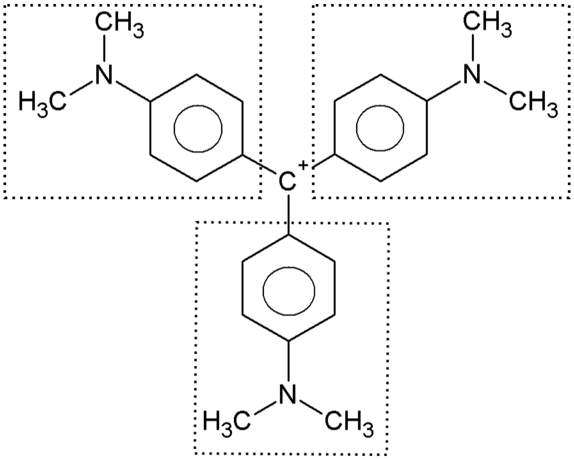

Figure 2.3: Chemical structure of Crystal Violet, a triphenylmethylene dye. Dashed rectangles denote aniline groups with the ability to rotate around the C^+-C bond.

The theory that supports the Förster-Hoffmann equation starts with the Debye-Stokes-Einstein (DSE) equation of diffusion. The phenyl groups of TPM dyes rotate according to the second order differential equation of molecular motion:

$$\theta\ddot{\varphi} + \chi\dot{\varphi} + \alpha(\varphi - \varphi_0^{'}) = 0 \qquad (2.4)$$

where θ is the rotational inertia of the phenyl groups, α represents the electrostatic force which returns the phenyl groups to its steady state position, φ_0 is the steady state equilibrium position, and φ is the angle deviation from φ_0 once the phenyl groups begin rotation. $\varphi(0)$ is assumed to be φ_0 and $\frac{d\varphi}{dt}$ =0 at t=0.

The microfriction factor χ, which represents the link to DSE microfriction, is related to the bulk viscosity η and can be written as:

$$\chi = 8\pi r^3 \eta \tag{2.5}$$

where r is the radius of the phenyl group. If the microfriction factor is high ($\chi^2 \gg 4\chi\theta$), then the return of phenyl groups to the planar state follows an exponential decay function, and the rate of deactivation is:

$$B(\varphi) = \beta(\varphi - \varphi_0)^2 \tag{2.6}$$

where β is a proportionality constant.

The probability of molecules being in an excited state can be written as:

$$-\frac{d\varrho}{dt} = \left(\frac{1}{\tau_0} + B(\varphi)\right)\varrho(t) = \left(\frac{1}{\tau_s} + \beta\delta\left(1 - e^{\left(\frac{-t}{\frac{X}{\alpha}}\right)}\right)^2\right)\rho(t) \tag{2.7}$$

where τ_s is the lifetime of a fluorophore at steady state, and ρ is the angular difference between excited and ground states.

Following the integration of previous equation, fluorescent quantum yield can be written as:

$$\phi = \frac{1}{\tau_s}\int_0^\infty \varrho(t)dt = \frac{\tau_0}{\tau_s}\int_0^\infty e^{-x-m-x^3}dx \tag{2.8}$$

where τ_0 is the natural lifetime.

Expression m is written as:

$$m = \sqrt{\frac{\beta\delta^2\tau_0^2}{3(\frac{X}{\alpha})^2}} \tag{2.9}$$

where σ is a dye dependent constant combining terms α, β, δ, and τ_0. If m is much smaller than 1, fluorescence is dominant and the previous equation can be rewritten as:

$$\phi = \frac{1 - \frac{6\sigma^2}{\eta^2}}{\frac{\tau_s}{\tau_0}} \tag{2.10}$$

and when m is much larger than 1 and $\eta \gg \sigma$, rotational relaxation is dominant:

$$\phi = \frac{\tau_0}{\tau_s} 0.893 \left(\frac{\eta}{\sigma}\right)^{\frac{2}{3}} \tag{2.11}$$

where all of viscosity independent variables are incorporated into a dye-dependent constant σ:

$$\sigma = \sqrt{\left(\frac{\alpha^2 \beta \delta^2 \tau_s^3}{192\pi^2 r^6}\right)} \tag{2.12}$$

Equation 2.11 can be simplified to the well known empirical form:

$$\phi = C\eta^x \tag{2.13}$$

where ϕ is quantum yield, proportionality constant C=0.893 $\frac{\tau_s}{\tau_0}\sigma^{-\frac{2}{3}}$, and dye dependent constant x=2/3 [3]. In solvent where $\eta \gg 1$, viscosity dominates, while in solvents with low viscosity, polar-polar interactions and friction dominate. In the latter case, x $\neq \frac{2}{3}$ is possible because of the two competing effects of steric hindrance and polar interactions [17].

Chapter 3

Instrumentation

3.0.1 SLR Camera

Digital SLR (single lens reflex) cameras represent a group of digital cameras which often have integration capability and sufficient sensitivity. A Konica Minolta SLR camera was examined in order to determine the sensitivity of its red, green, and blue (RGB) channels. Camera's lens was removed, and the camera placed inside a spectrofluorophotometer where a light beam was projected onto its light sensor. After the intensity of the light beam was collected, it had to be normalized by dividing it with the spectrofluorophotometer's reference signal, and the resulting sensitivities of the camera's RGB channels is shown in Figure 3.1. The intensity maximum between the region defined by the first contour line and the region defined by the second contour line is reduced to 93.8 % of the maximum.

To ascertain the homogeneity of LED light illumination on cotton bolls, an image of white paper was taken at aperture f/11 and automatic exposure time. A false colored image is shown in Figure 3.2, where the dashed rectangle indicates the approximate position of cotton bolls during imaging.

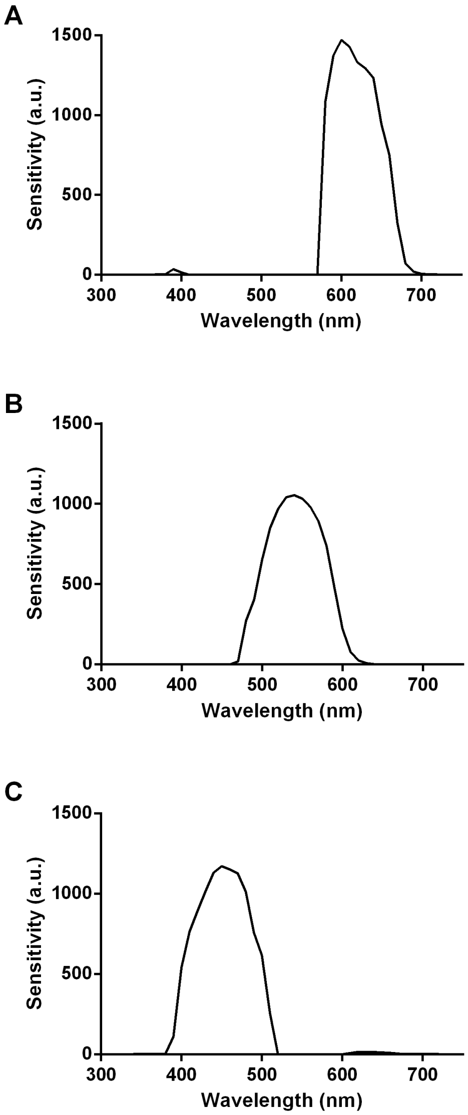

Figure 3.1: Camera sensitivity of its red (A), green (B), and blue (C) channel. Intensity of a light beam shined onto the camera's sensor was collected and normalized by dividing it with the spectrofluorophotometer's reference signal.

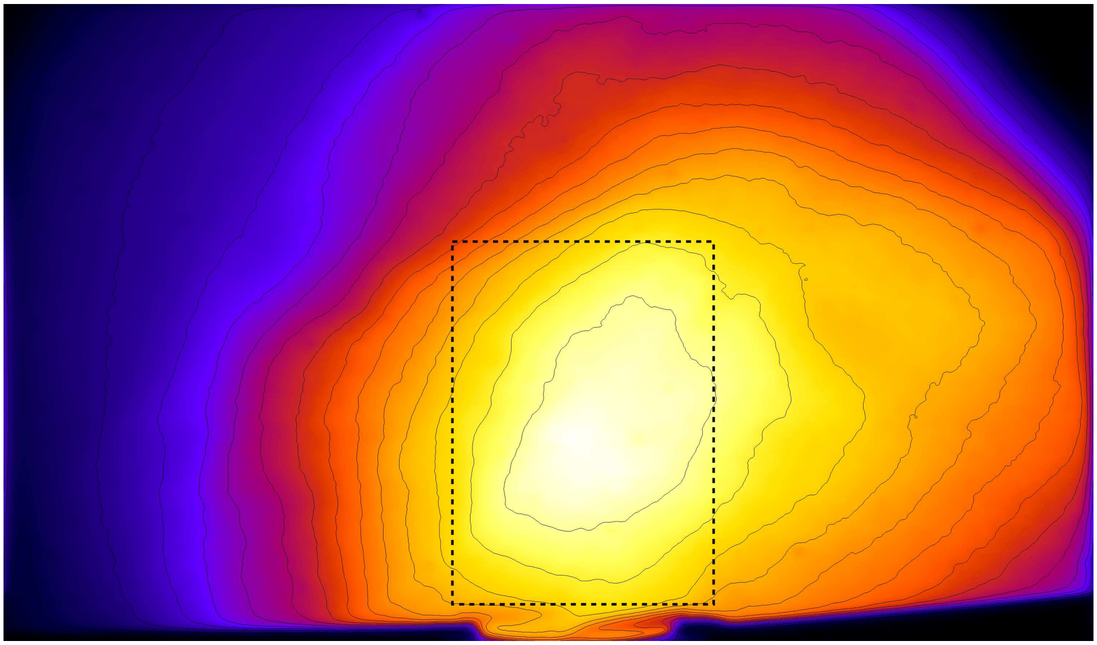

Figure 3.2: White paper illuminated with LED light. Dashed rectangle indicated the approximate position of cotton bolls during imaging. Intensity variation from the maximum of the first contour line to the second contour line is reduced to 93.8 %.

Chapter 4

Research Goals

The research presented in this dissertation concerns two areas: investigations of fundamental properties of molecular rotors with respect to their application of fluorescent imaging of flow patterns, and fluorescent imaging of cotton bolls to discern damage caused by stink bugs. A previous report by Mustafic et al. regarding molecular rotors in viscous solvents show a method where the solution was injected into flow chambers of various geometries with the flow rates controlled via a programmable syringe pump [5]. Photoexcitation was provided by two collimated LED sources, and images taken with an SLR camera. The results point to a shear sensitivity of molecular rotors, and fluorescent images showed their potential application as flow sensors with high spatial and temporal resolution. However, the mechanism behind this shear sensitivity remained unknown. To examine this phenomenon in greater detail, a spectroscopic system was constructed. An apparatus containing a quartz tubing was placed in a spectrofluorophotometer, and emission intensity of molecular rotors in various solvents under different shearing regimes examined.

The second goal was to examine applications of fluorescent imaging with regards to cotton bolls. Earlier records show that once cotton bolls are subject to stink bug infestation, they leave a unique fluorescent signature, with associated receding of chlorophyll [7]. Under

LED excitation, cotton bolls fluoresce red, and when stink bugs puncture through the outer wall with a proboscis, a certain amount of chlorophyll is removed. Once the chlorophyll is removed, the damaged area exhibits a blue/green fluorescence, and starts a process of degradation. This results in lint discoloration, and lowers its market value significantly. Since cotton is a major product in the U.S.A. and other countries, detection methods of stink bug infestation are invasive and don't provide an early when to apply insecticide. In this research, we developed a new method to detect stink bug damage in cotton, which is non-invasive and economical. The ultimate goal would be to incorporate this method into a device that can detect stink bug infestation of cotton bolls in the field.

Chapter 5

Molecular Rotors as Flow Sensors

A unique property of molecular rotors is the application in fluorescent imaging by spatially resolving its fluorescence emission, as explored in a recent study by Mustafic et al. [5]. The two molecular rotors used in this study were CCVJ and CPVDA. Both molecular rotors exhibit increased fluorescence intensity in viscous and polar solvents. Flow chambers constructed from polycarbonate and polyoxymethylene (commercial name Delrin) with 3 mm milled in channels of different geometries had a borosilicate glass slide glued on top of it. Flow chambers were positioned on a post in front of an emission filter. Two LED excitation sources provided a homogeneous illumination, while images were taken with a digital SLR camera.

10 μM solutions of CCVJ(9-[(2-Cyano-2-hydroxy carbonyl)vinyl]julolidine) and CPVDA(p-[(2-cyano-2-propanediol ester)vinyl]dimethylaniline), shown in Figure 5.1, were made with a viscous solvent, ethylene glycol. The solution was thoroughly mixed and placed in syringe pump. Polyethylene tubing connected the syringe to the flow chamber inlet, while another piece of polyethylene tubing connected the flow chamber to an empty syringe collecting excess fluid.

All images were taken with lens aperture f/2.8 and exposure time of 8 s. The camera

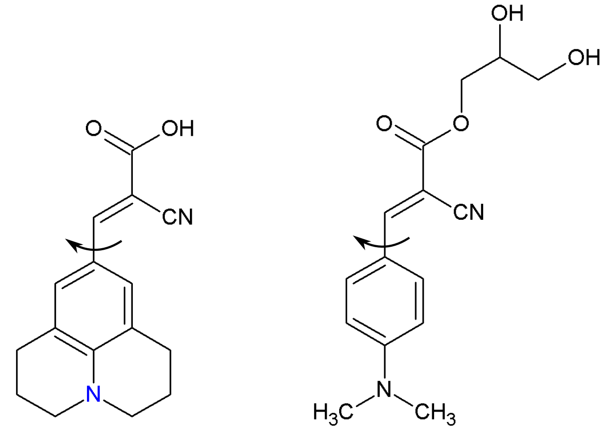

1 **2**

Figure 5.1: Chemical structure of molecular rotors **1** (CCVJ) and **2** (CPVDA). Arrows denote axis of rotation.

acquired raw images at 0.25, 0.50, 0.75, 1.00 and 1.50 ml/min flow rate, with each flow rate imaged at flow and while at rest. Raw images were converted to TIFF images, and extracted blue channel converted to a grayscale image. This was followed with image binning and noise reduction. Normalized images were created by using no flow images in order to eliminate background inhomogeneities, and followed by additional denoising. An example of spatially resolved fluorescence emission in the hexagonal chamber geometry is shown in Figure 5.2.

An increasing flow rate can be seen from images, with an increasing flow rate top to bottom. Average intensities of a rectangular region in the center of the chamber were calculated, and plotted as a function of flow rate, as seen in Figure 5.4. As the flow rate increases, so does the average intensity, albeit in a non-linear fashion. At the lowest flow rate of 0.25 ml/min, fluorescence emission barely visible near the inlet. From 0.50 ml/min to 1.50 ml/min fluorescence intensity increases, and saturates at 1.50 ml/min. Flow chamber geometry shown in Figure 5.3 pairs well with a computed fluid velocity simulation. Emission

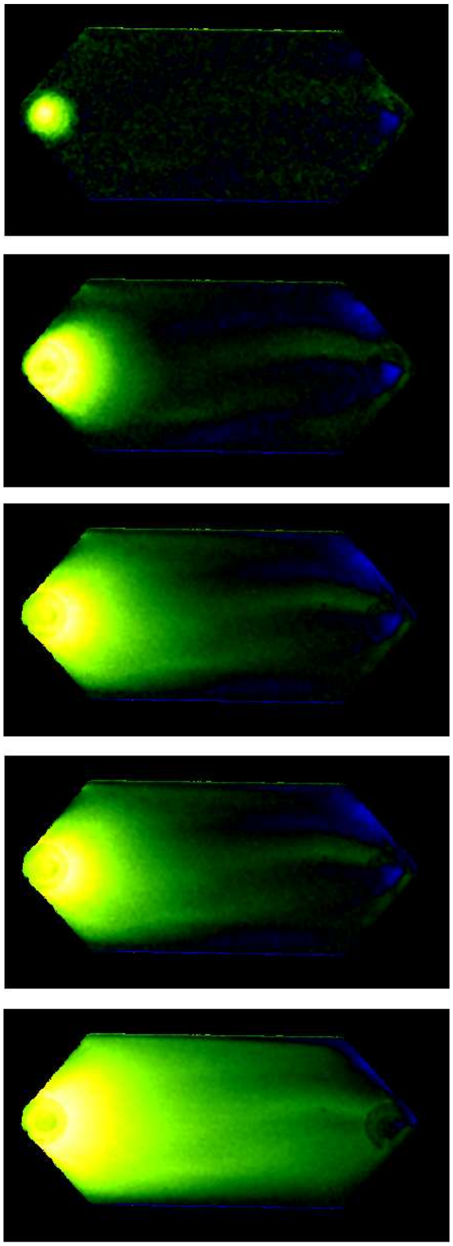

Figure 5.2: Spatially resolved fluorescence emission images of CCVJ in ethylene glycol at 0.25 ml/min (top) and increasing to 1.50 ml/min (bottom) [5].

intensity is higher in the inlet region where the flow rate is highest and lower in the wide basin region.

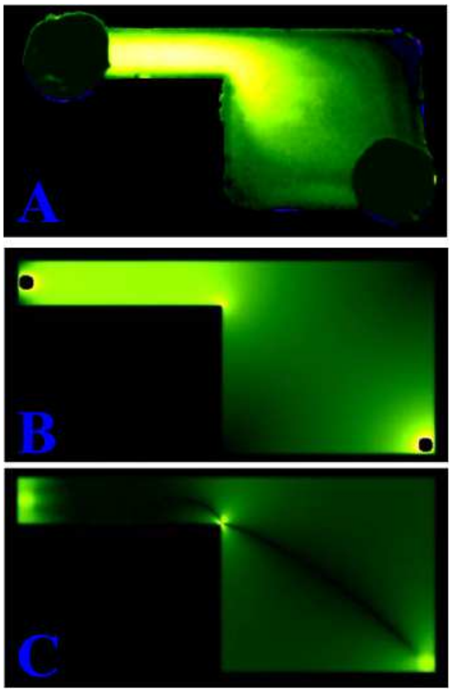

Figure 5.3: Spatially resolved emission intensity of CCVJ in ethylene glycol at 1 ml/min (A), and a computed fluid dynamics simulation of the chamber depicted in A, showing projected fluid velocity (B) and projected fluid shear stress C [5].

A curve fit of the non-linear relationship between fluorescence intensity and flow rate for CCVJ and CPVDA is shown in Figure 5.5. The observed intensity increase is much higher for CCVJ than CPVDA, and also approaches the saturation rate much faster.

This study illustrates the capabilities of molecular rotors to be used in fluorescent imaging due to their flow sensitivity. The method has a high temporal and spatial resolution, and is affordable when compared to other flow measurement techniques. Under induced shearing, both molecular rotors in ethylene glycol show an increased fluorescent quantum yield, and flow pattern images were qualitatively compared with computed flow profiles. However, only one solvent was used in this study, and the question whether fluid velocity or shear stress

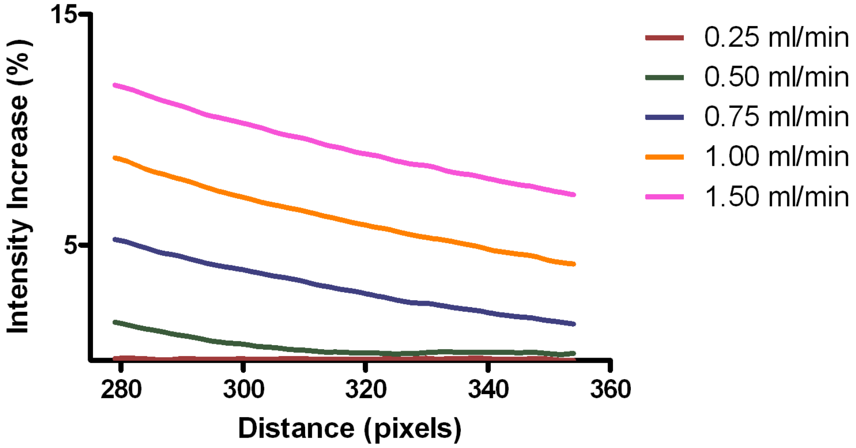

Figure 5.4: Average fluorescence intensity of CCVJ in ethylene glycol from a selected region in the center of the hexagonal chamber geometry [5].

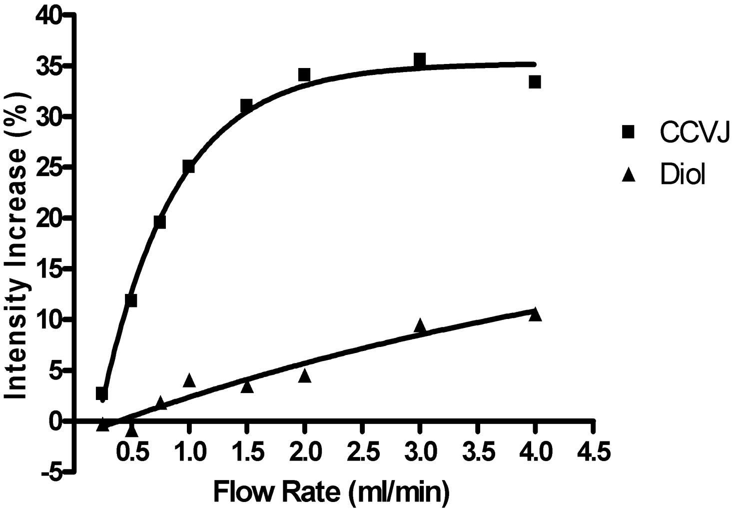

Figure 5.5: Flow rate vs. intensity increase for CCVJ and CPVDA in ethylene glycol in a selected rectangular region of the hexagonal chamber geometry [5].

causes the intensity needs to be further explored with additional experiments with molecular rotors in different solvents.

Chapter 6

Shear Sensitivity of Molecular Rotors in Selected Solvents

6.1 Introduction

Molecular rotors represent a subgroup of fluorescent dyes known for their unique properties and functionalities. More specifically, they form twisted intramolecular charge transfer (TICT) arrangements which occur following the molecular rotors' photoexcitation from the ground state to the excited state [12]. Subsequent to the cessation of photoexcitation and following the photon absorption, molecular rotors return to the ground state via two mutually exclusive pathways: fluorescence emission or non-radiative molecular rotation [14]. Intramolecular rotation is the dominant pathway in solutions of low viscosity, while in solutions of high viscosity, fluorescence emission is the dominant pathway [18, 19].

Molecular rotors consist of an electron donor unit and an electron acceptor unit, at whose junction can be found an electron-abundant π system conjugation which during the non-radiative molecular rotation plays an essential role, namely allowing the rotation of one segment of a molecular rotor with respect to the other segment around the covalent σ bonds.

The π system serves two main purposes in this context: it prevents overlap between σ and π orbitals from the donor and acceptor group due to spatial isolation, and to facilitate the movement of donor electrons to the empty acceptor orbitals. The movement of electrons from the σ and π orbitals to the antibonding σ^* and π^* states is accompanied by an energy gain due to excitation to a higher energy level [4, 20].

The quantum yield produced by molecular rotors during its return to the ground state is dependent on the viscosity of solvent and can be described by the Förster-Hoffmann equation:

$$\phi = C \cdot \eta^x \tag{6.1}$$

where ϕ is quantum yield, C and x are dye dependent constants and η is viscosity [3, 12].

Recently, research in the area of molecular rotors has produced a number of cases where molecular rotors can be used for a variety of purposes, namely as fluorescent non-mechanical viscosity sensors [21], real-time viscosity sensing in liposome systems [22], design of amyloid imaging molecular rotors as a new tool for Alzheimer's disease and other neurodegenerative disorders [23].

Research by Haidekker et al. has shown that when solutions of polar molecular rotors and polar solvents are subjected to shear stress, an increased intensity can be observed [24]. A subsequent study by Mustafic et al. has provided strong evidence that polar-polar interactions between fluorophore and solvent create a flow sensitive effect, whereby an increase in fluorescence intensity is caused by flow rather than shear stress [5].

To examine the question of the shear sensitivity mechanism, three molecular rotors shown in Fig.6.1 were utilized for the making of solution mixtures: **1** (CCVJ: (9-(2-carboxy-2-cyanovinyl)-julolidine))(Sigma, St. Louis, MO), **2** (CCVJ-TEG: (9-(2-carboxy-2-cyanovinyl)-julolidine) triethyleneglycol ester)), and **3** (CPVDA: (p-[(2-cyano-2-propanediol ester) vinyl] dimethylaniline)), both synthesized by our group. The solubility of molecular rotors in solvents is determined by the presence or absence of functional groups. In this instance molecular rotor **1** has one -OH group, **2** has a triethyleneglycol group, and **3** has two -OH groups. These functional groups determine their solubility when solvated in polar solvents, and because of this property, determine the molecular rotors' ability to form hydrogen bonds.

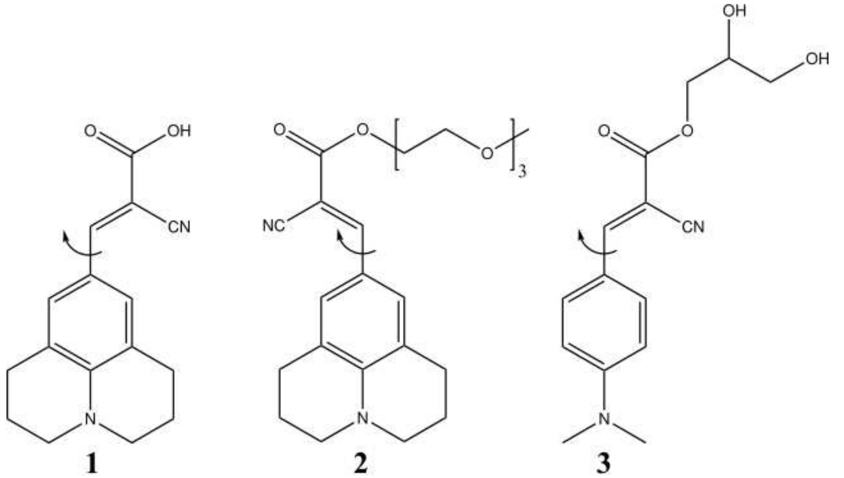

1 **2** **3**

Figure 6.1: Chemical structures of molecular rotors **1** (CCVJ: (9-(2-carboxy-2-cyanovinyl)-julolidine)), **2** (CCVJ-TEG: (9-(2-carboxy-2-cyanovinyl)-julolidine) triethyleneglycol ester)), and **3** (CPVDA: (p-[(2-cyano-2-propanediol ester) vinyl] dimethylaniline)). Arrows denote the axis of rotation of 2-cyanoprop-2-enoic acid group with respect to the julolidine group (in the case of CCVJ and CCVJ-TEG) and the aniline group (in the case of CPVDA) during radioationless deexcitation from the locally excited (LE) planar state.

While the phenomenon of molecular rotor shear sensitivity and fluorescence emission in viscous solvents has been observed, so far no theoretical explanation exists. The purpose of this paper is to elucidate additionally the basis for their basic mechanism and behavior, and we hypothesize that polar-polar interactions between the molecular rotors and solvents play an important role in it.

6.2 Materials and Methods

6.2.1 Stirrer experiment

A 10 μM solution of a molecular rotor in ethylene glycol was placed in a fluoroscopic cuvette, and a stir bar introduced at a moderate speed, and a fluorophotometer recorded emission spectra. In the case of a 10 μM solution of CCVJ in EG, this was followed by closing of the fluorophotometer's slits, while replacement excitation light was provided by an LED (Philips/Luxeon LXHL-LR5C) with a bandpass filter (D450/40) attached to it. Emission spectra was measured at a 3nm slit with a DCLP475 filter in front of emission detector.

6.2.2 Apparatus Construction and Solution Injection

The apparatus shown in Fig.6.2 was constructed from two thin sheets of aluminium, held together in place by four steel poles (Thorlabs, Newton, NJ). The two sheets have a centrally located holes of approximatelly 7 mm in diameter, through which a quartz tubing, which has better optical properties than regular glass, (4 mm outer diameter) (Technical Glass Products, Painesville Twp., OH) was inserted. The quartz tubing inlet was connected to teflon tubing (Restek Corp., Bellefonte, PA) via a two way connector (Omnifit, Danbury, CT), which in turn was attached to a syringe (Eisele Interchange, Nashville, TN) which delivered variable flow rates. The syringe delivered programmable flow rates for predetermined periods of time via a custom syringe pump. The quartz tubing outlet was connected via a two way connector to teflon tubing which in turn was attached to an empty syringe cylinder to collect excess fluid accumulated during solution pumping. Teflon was chosen because solvents like DMSO cannot dissolve it, and it has low coefficient of friction.The entire apparatus was placed in the sample chamber of a fluorophotometer (Fluoromax 3 Jobin-Yvon, Edison, NJ) and completely isolated from light, although the teflon tubing protruded from it.

Solutions were mixed throughout by combining 50 μl of a 10 μM stock solution of molec-

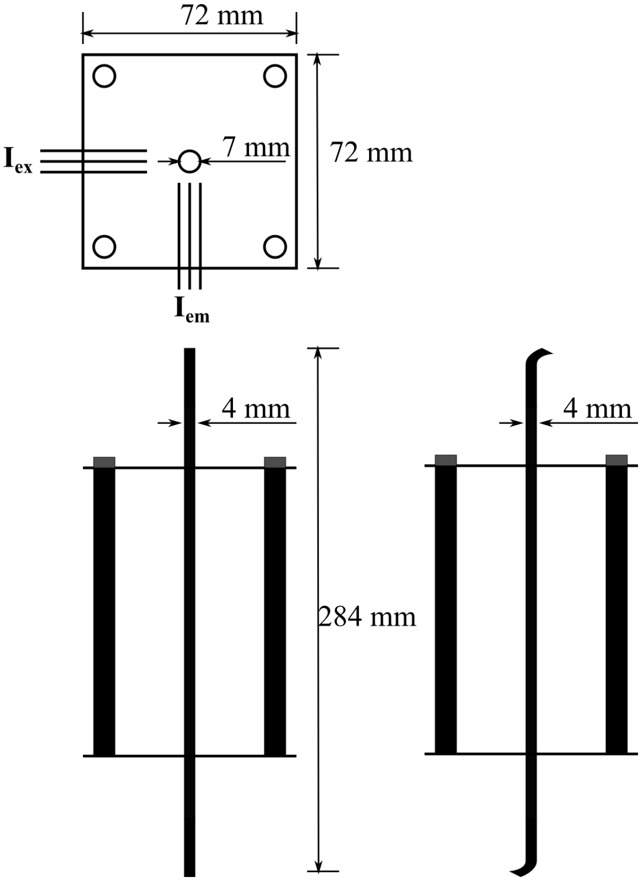

Figure 6.2: Top, front and side view of an assembly holding quartz tubing through which solution mixtures of selected solvents and molecular rotors were injected. The entire apparatus was placed in a spectrofluorometer chamber and firmly attached to bottom holding posts. Quartz inlet and outlet were attached to teflon tubing via 2-way connectors. One end of teflon tubing was connected to a syringe delivering solutions under different flow rate routines, while the other end was attached to an empty syringe cylinder collecting excess solutions.

ular rotors with 50 ml of selected solvents: ethylene glycol (EG), methanol (MeOH), toluene, and dimethyl sulfoxide (DMSO). After the solution was prepared, a 50 ml syringe was filled with it and placed in a holder attached to a custom syringe pump, and attached to teflon tubing inlet via a Luer-Lok connector.

6.2.3 Intensity Recovery

A 10 μM solution of molecular rotor **1** in ethylene glycol and DMSO, respectively, was placed in a fluoroscopic cuvette. Emission spectra was recorded with the solution at rest. This was followed by an addition of a stir bar, which was activated and emission spectra recorded. Initially, emission spectra were recorded while the solutions were at rest, and then repeated over a period of 7 hours while the solution was stirred.

6.2.4 Timecourse Scan Analysis

Solutions of molecular rotors and solvents (total of 12, including 3 molecular rotors and 4 solvents) were injected from a syringe at programmable flow rates of 0.25, 0.50, 0.75, 1.00, 2.00, 3.00 and 4.00 ml/min, controlled by a custom syringe pump, and fluorophotometer recorded 3 timecourse scans for each solution to ensure repeatability. A representative scan of a 10 μM solution of molecular rotor **1** in ethylene glycol (number of repeats N=3) is shown in Fig. 6.3 where aforementioned flow rates were applied to the respective solution with the addition of a region marked refill, during which the syringe was refilled after being emptied out of solution. Before each flow rate was applied, a steady baseline was established for approximatelly 300 seconds during which no solution was injected.

To analyze the relative intensity increase during a selected flow rate the following operations were performed as shown in Fig. 6.4, which shows a timecourse scan of a 10 μM solution of molecular rotor **1** in ethylene glycol at a flow rate of 0.50 ml/min. The steady-state baselines before and after the solution was sheared are marked by b_1 and b_2, while s designates the region of peak intensity during shearing. Averages for regions b_1 and b_2 were computed, and subtracted from the average for region s, as shown in equation 6.2:

$$\Delta I = s - \frac{b_1 + b_2}{2} \tag{6.2}$$

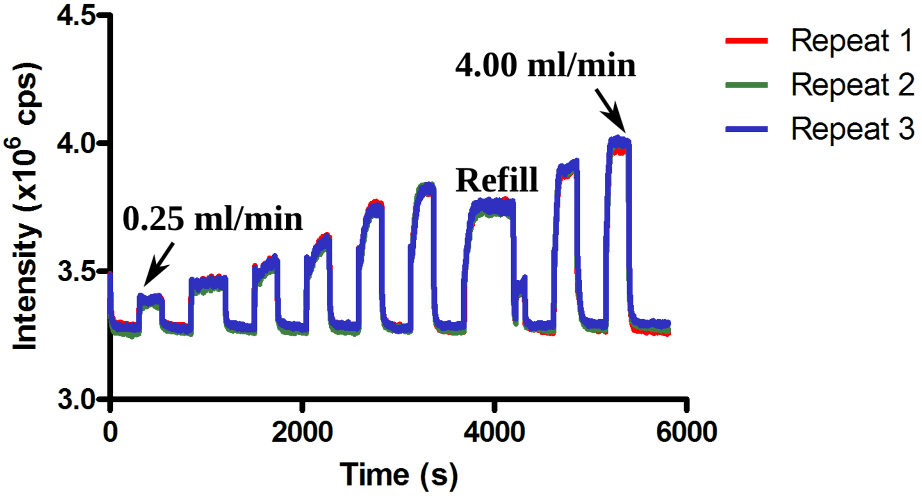

Figure 6.3: A timecourse scan of a 10 μM solution of molecular rotor **1** in ethylene glycol (N=3) with noticeable intensity increases everytime a higher shear rate was applied, thus indicating a positive relation between the two until a saturatiion level was achieved at higher flow rates. Flow rates of 0.25, 0.50, 0.75, 1.00, 1.50, 2.00, 3.00 and 4.00 ml/minute were applied. Syringe was refilled between flow rates 2.00 and 3.00 as indicated in the figure.

where ΔI represents the relative intensity increase in counts per second.

6.3 Statistical Analysis

The data for intensity increase was calculated using Equation 6.2, and plotted as a function of flow rates. Statistical analysis software utilized to determine curve-fit parameters was GraphPad Prism v.4 (GraphPad Software, Inc., La Jolla, CA 92037). The resulting data was subject to two different types of curve-fits, that is Boltzmann sigmoidal (Eq. 6.3) and exponential association (Eq. 6.4).

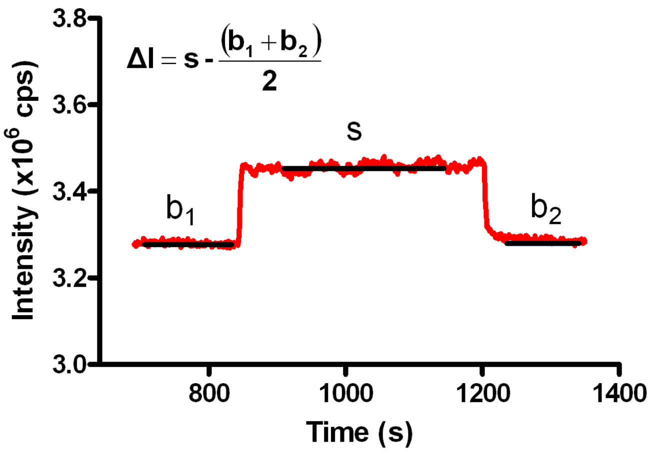

Figure 6.4: A selected region of a timecourse scan of 10 μ M molecular rotor **1** in ethylene glycol extracted from Figure 6.3. Baselines b_1 and b_2 show regions before and after a flow rate of 0.50 ml/min was applied, and s shows a region of increased intensity during shearing. The intensity increase ΔI was calculated by subtracting the average of intensity during shearing s from the average of baselines b_1 and b_2 during which the solution was at rest. In this instance ΔI=0.165 and $\Delta I_{norm} = 0.05$.

The Boltzmann sigmoidal equation can be written as:

$$\Delta I = \Delta I_{max} \cdot \frac{1}{1 + e^{\frac{V50 - V}{slope}}} \tag{6.3}$$

where ΔI is the flow dependent intensity increase, ΔI_{max} is the maximum intensity increase at the largest value of flow rate, V50 is the flow rate when intensity increase is halfway between the smallest (in this case 0) and the largest value for intensity increase, and V is the variable flow rate.

The exponential association equation can be written as:

$$\Delta I = \Delta I_{max} \cdot \left(1 - e^{-\frac{V}{V_0}}\right) \tag{6.4}$$

where V_0 is the fitting constant.

Equation 6.5 represents a normalized version of Equation 6.4 where I_{norm} is the flow dependent intensity increase during shearing which was normalized by dividing it with baseline values for steady state intensity in the absence of flow, and the relative intensity increase δI showing by how much the baseline intensity is exceeded was calculated using the following equation:

$$\delta I = I_{norm} \cdot \left(1 - e^{-\frac{V}{V_0}}\right). \tag{6.5}$$

Following curve fitting, the two statistical model were subjected to Akaike Information Criteria (AIC) to determine their goodness of fit and see which is more suitable. Exponential association was the preferred model in 8 cases (molecular rotor **1** in EG, molecular rotor **2** in EG, molecular rotor **3** in EG, molecular rotor **1** in MeOH, molecular rotor **2** in MeOH, molecular rotor **2** in Toluene, molecular rotor **2** in DMSO, molecular rotor **3** in DMSO), while Boltzmann sigmoidal was the preferred model in 2 cases (molecular rotor **1** in Toluene, molecular rotor **3** in Toluene). Since the statistical model preferred in most cases was exponential association, it was decided to use it for curve fitting our data sets.

6.4 Results

6.4.1 Stirrer Experiments

To observe emission intensity changes at rest and while being stirred, emission spectra of a 10 μM solution of molecular rotor **1** in ethylene glycol was recorded, and it shows a 15 % emission intensity increase at peak wavelength during stirring at a modest speed (Figure 6.5). Two additional stirrer experiments were done with solutions of molecular rotor **4** in EG, and molecular rotor **5** in EG (chemical structures shown in Figure 6.7). Fluorophotometer's excitation light was occluded and the experiment repeated while a homogeneous excitation light was provided with a blue LED which illuminated the entire cuvette (Figure 6.6). At the emission peak of 486 nm, there was no observable emission intensity at rest or during stirring.

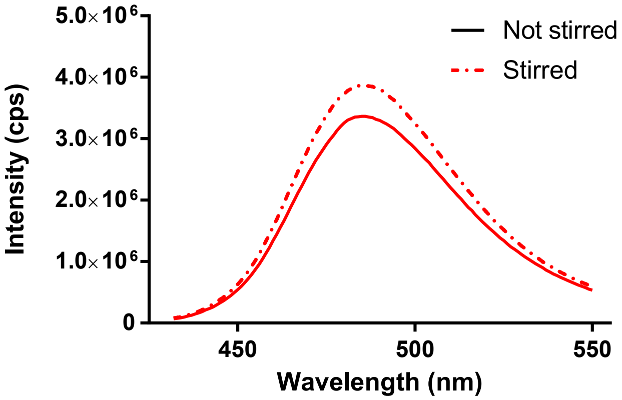

Figure 6.5: Emission intensity of a 10 μM solution of molecular rotor **1** in ethylene glycol at rest and while stirred. Peak wavelength emission intensity increased 15 % during shearing [5].

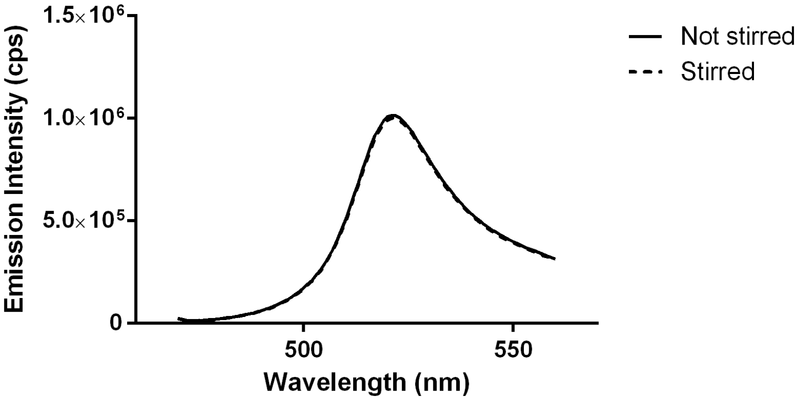

Figure 6.6: Emission intensity of a 10 μM solution of molecular rotor **1** in ethylene glycol when the whole cuvette is illuminated with an LED. There is no emission intensity increase at the emission peak of 486 nm, at rest or while being stirred.

Emission spectra a 10 μM solution of molecular rotor **1** in ethylene glycol (measured at 3/3 nm slits at peak wavelength of 485 nm) and DMSO (measured at 5/5 nm slits at

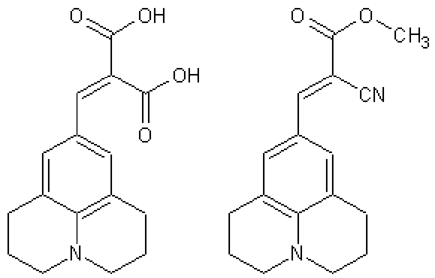

4 **5**

Figure 6.7: Chemical structures of molecular rotors **4** ((2,3,6,7-tetrahydro-1H,5H-pyrido[3,2,1,-ij]quinolin-9-ymethylidene)propanedioic acid) and **5** (CCVJ-methylester).

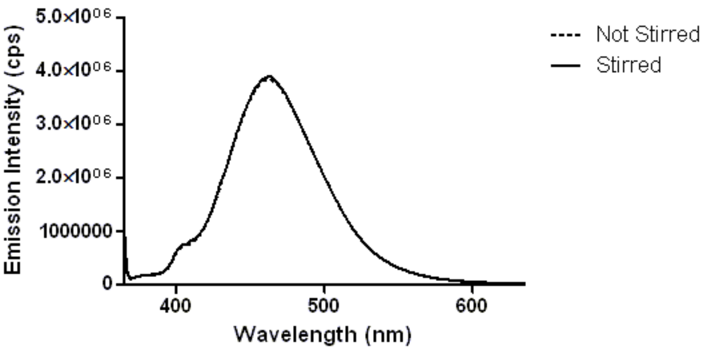

Figure 6.8: Emission intensity of a 10 μM solution of molecular rotor **4** in ethylene glycol at rest and while stirred. Peak wavelength emission intensity did not increase during shearing.

peak wavelength of 484 nm), respectively, is shown in Figure 6.10. For molecular rotor **1** in ethylene glycol, emission intensity at rest compared to the emission of the stirred solution after 7 hours in the dark increased by 16 %, while for molecular rotor **1** in DMSO, emission intensity increased by 27 %.

6.4.2 Timecourse Scans

After the injection of a solution begins it takes several seconds before the plateau peak is reached and maintained during shearing. Following the end of shearing, the timecourse scan

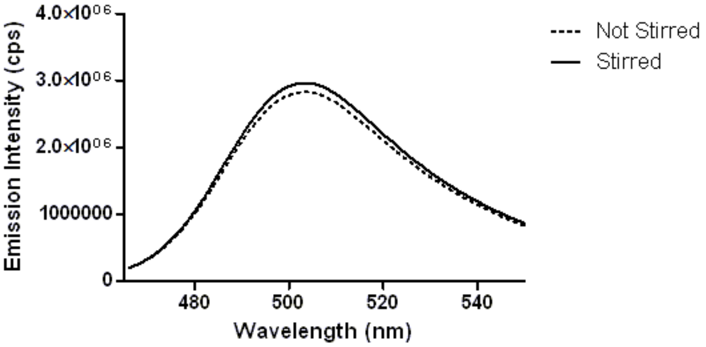

Figure 6.9: Emission intensity of a 10 μM solution of molecular rotor **5** in ethylene glycol at rest and while stirred. Peak wavelength emission intensity increased 5 % during shearing.

reaches the steady state baseline. Exponential association of timecourse data is shown in Fig. 6.11 and curve fit parameter values in Table 6.1. In ethylene glycol, the values for ΔI_{max} were the highest for molecular rotor **2** (2293), followed by molecular rotor **1** (1960) and molecular rotor **3** (1457). The characteristic flow rate V_0 is highest in molecular rotor **2** (2.877), then molecular rotor **3** (2.156) and molecular rotor **1** (1.826). In methanol, results followed the same pattern, with molecular rotor **2** having higher ΔI_{max} and V_0 (154, 4.5) than molecular rotor **1** (94.14, 1.201). In DMSO, molecular rotor **3** has the highest values for ΔI_{max} (352.4) than molecular rotor **2** (321.4), while the values for V_0 were marginally smaller (1.003 vs. 1.005). In toluene, ΔI_{max} for molecular rotor **1** (772376) was much higher than in molecular rotor **3** (14314) and molecular rotor **2** (193.6), and V_0 much higher in molecular rotor **3** (333.33) than molecular rotor **2** (3.045) and molecular rotor **1** (1.09x10^{-6}).

Average intensity for each flow rate was normalized by dividing it with its baseline and exponential association curve fitted (Fig. 6.5). ΔI_{norm} (in %) shows by how much applications of each succeeding flow rate exceeded the baseline values established during steady state. In polar solvent EG, gains were the highest for ΔI_{norm} (molecular rotor **1**=0.596,

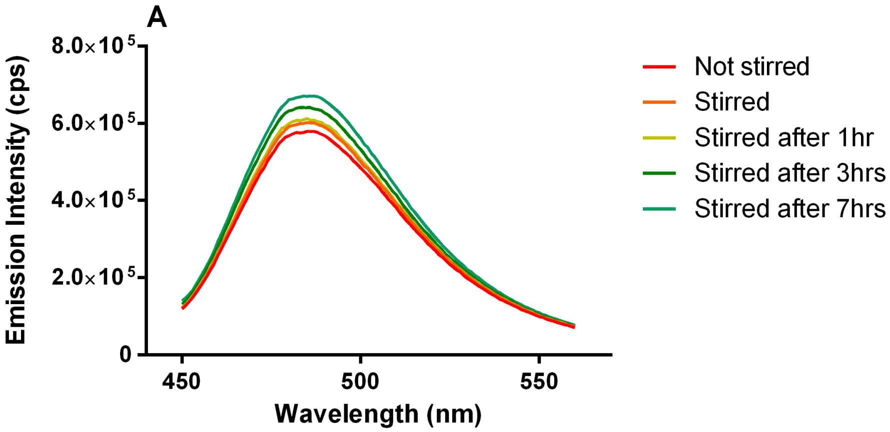

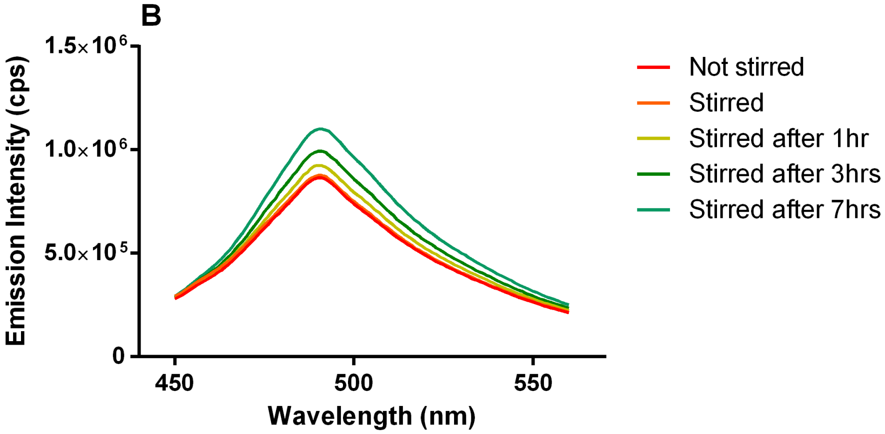

Figure 6.10: Emission intensity of a 10 μM solution of molecular rotor **1** in ethylene glycol (A) and DMSO (B), respectively.

molecular rotor **2**=0.547, molecular rotor **3**=0.558), exceeding those in the other polar solvent MeOH (molecular rotor **1**=0.123, molecular rotor **2**=0.133). In dipolar aprotic solvent DMSO, ΔI_{norm} values were the lowest (molecular rotor **2**=0.105, molecular rotor **3**=0.195). In non-polar toluene, reflecting the preference for Boltzmann sigmoidal curve fit, values for

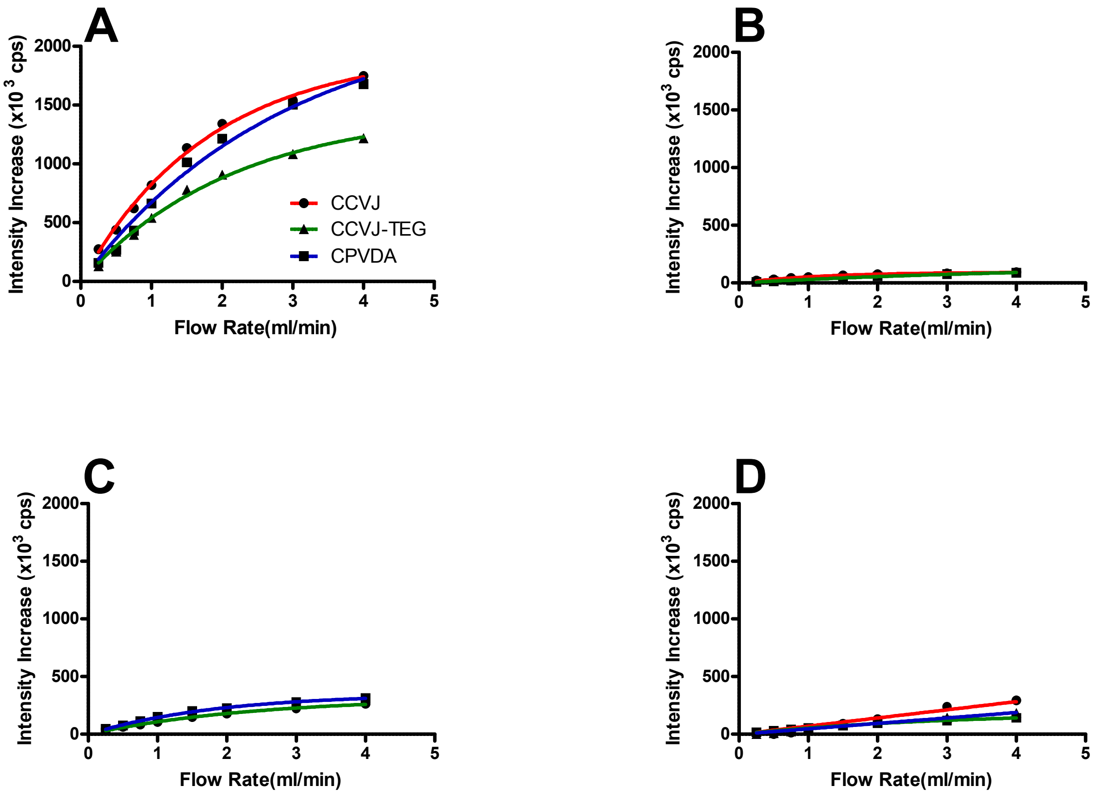

Figure 6.11: Exponential association curve fit of selected molecular rotors in A) ethylene glycol, B) methanol, C) dimethyl sulfoxide and D) toluene.

ΔI_{norm} were very high in two cases: molecular rotor **1** (244.8) and molecular rotor **3** (5.435), while for molecular rotor **2** were more reasonable (0.111). The highest characteristic flow rate V_0 in EG was recorded for molecular rotor **3** (2.877), then molecular rotor **2** (2.156) and molecular rotor **1** (1.678). Conversely, in MeOH molecular rotor **1** had the lowest V_0 (1.201), but was higher in molecular rotor **2** (4.50).

DMSO exhibited the highest V_0 in molecular rotor **2** (2.431) followed by molecular rotor **3** (1.869). In toluene V_0 was the highest in molecular rotor **3** (301.2), followed by molecular rotor **2** (3.045) and molecular rotor **1** ($1.09\text{x}10^{-6}$). In two cases: molecular rotor **3** in MeOH

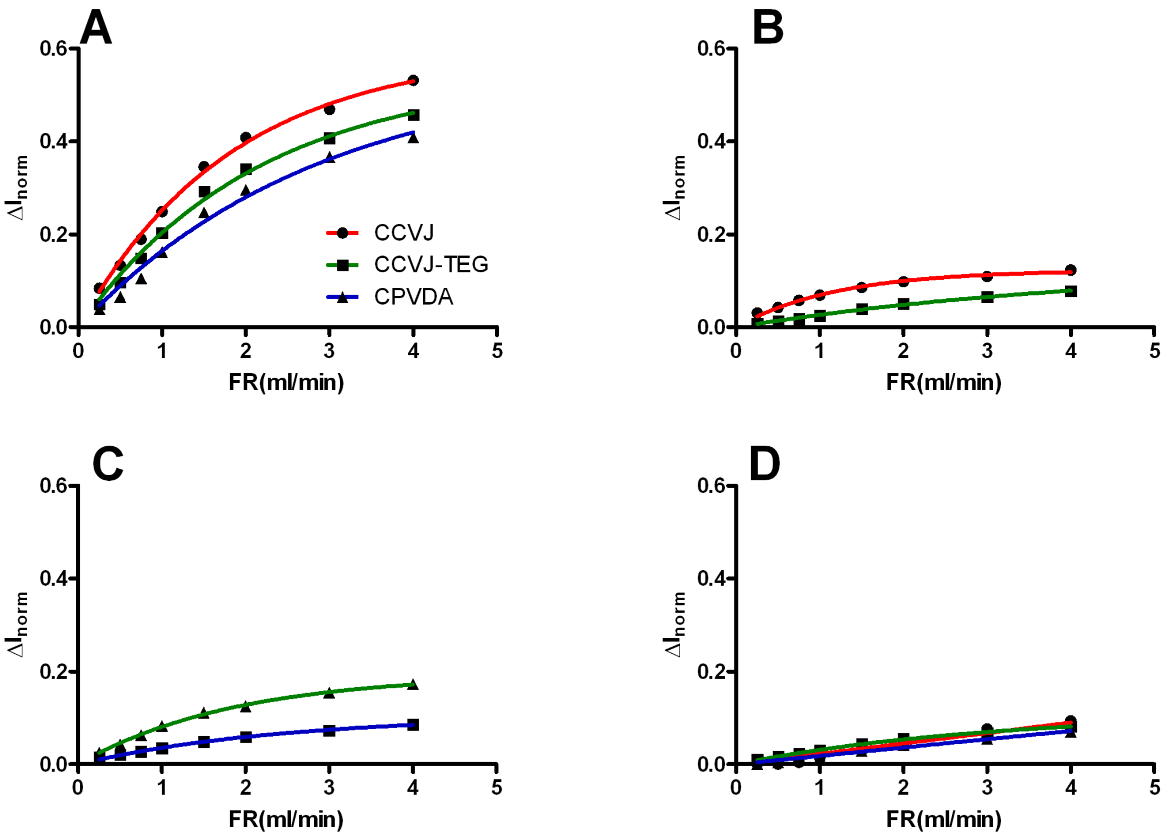

Figure 6.12: Normalized exponential association curve fit of selected molecular rotors in A) ethylene glycol, B) methanol, C) dimethyl sulfoxide and D) toluene. I_{norm} (%) is the flow dependent intensity increase during shearing which was normalized by dividing it with baseline values for steady state intensity in the absence of flow.

and molecular rotor **1** in DMSO (Fig.6.13) it wasn't possible to analyze data due to the absence of repeatability and steady state baseline, unlike the case of molecular rotor **1** in EG (Fig.6.3). Graph of ΔI_{norm} values for solvents EG, MeOH and DMSO is shown in Fig. 6.14 stand in close proximity to each other in their respective solvents.

Table 6.1: Normalized and non-normalized parameter values obtained from exponential curve fit of data. (* represents the case shown in Fig. 6.13 and others where the relation between shearing and intensity doesn't exist, and hence the statistical analysis wasn't possible).

Solvent	**Variables**	**Mol. Rotor 1**	**Mol. 2**	**Mol. Rotor 3**
Ethylene glycol	ΔI_{max}	1960	2293	1457
	ΔI_{norm}	0.596	0.547	0.558
	$\frac{1}{V_0}$	0.548	0.348	0.464
	R^2	0.996	0.986	0.993
	V_0	1.826	2.877	2.156
Methanol	ΔI_{max}	94.14	154	*
	ΔI_{norm}	0.123	0.133	*
	$\frac{1}{V_0}$	0.833	0.222	*
	R^2	0.987	0.995	*
	V_0	1.201	4.500	*
DMSO	ΔI_{max}	*	321.4	352.4
	ΔI_{norm}	*	0.105	0.195
	$\frac{1}{V_0}$	*	0.411	0.535
	R^2	*	0.995	0.998
	V_0	*	1.005	1.003
Toluene	ΔI_{max}	772376	193.6	14314
	ΔI_{norm}	244.8	0.111	5.435
	$\frac{1}{V_0}$	$9.16\text{x}10^{-5}$	0.328	0.003
	R^2	0.942	0.998	0.976
	V_0	$1.09\text{x}10^{-6}$	3.045	333.33

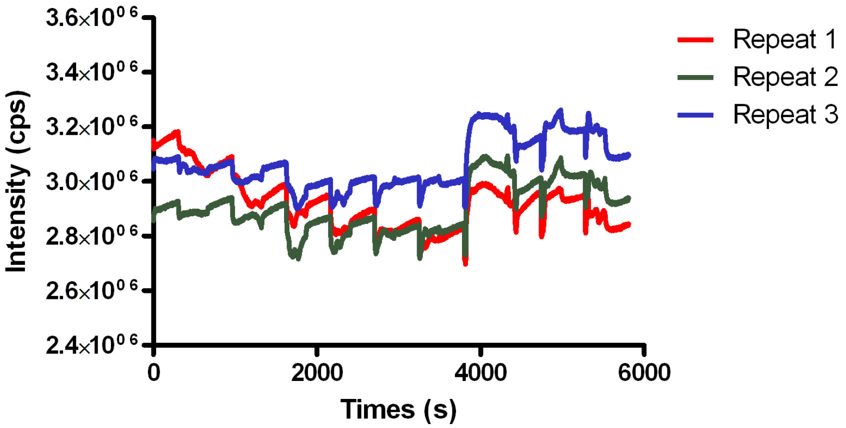

Figure 6.13: A timecourse scan of a 10 μM solution of molecular rotor **1** in dimethyl sulfoxide (N=3) where the relation between increasing flow rates and increasing intensity increase during (as shown in Fig. 6.3) shearing doesn't exist. The timecourse scans during three repeats show a much larger variation than those seen in Fig. 6.3 and the steady state baseline in the absence of flow wasn't established.

6.5 Discussion

To further explore the behavior of molecular rotors in different microenvironments and how they influence the TICT state formation and fluorescence emission, a selection of four solvents (ethylene glycol, methanol, dimethyl sulfoxide, and toluene) were chosen based on their intrinsic properties which determine interactions with atoms from molecular rotors and are shown in Table 6.2. This was done in order to understand whether polar-polar interactions plays an important role in interactions between molecular rotors and solvents. Following the analysis of timecourse data and normalization it was necessary to model the fluorescence intensity response. While no theoretical basis exists, the fluorescence intensity response of molecular rotors in solutions was modeled with two curve fits, typically found in low order systems, namely the Boltzmann sigmoidal (Eq. 6.3) and exponential association (Eq. 6.4).

Ethylene glycol and methanol are polar protic solvents, meaning they have the ability to

Table 6.2: Properties of solvents used in this study [8].

Solvent	**Dipole Moment**	**Molecular Weight**	**Viscosity η (25°C) [mPa·s]**	**Dielectric Constant ε**	**Polarity**
Ethylene glycol	2.36	62.068	16.06	41.40	Polar protic
Methanol	1.70	34.042	0.54	33.00	Polar protic
Dimethyl sulfoxide	3.96	78.133	2.47	48.90	Dipolar aprotic
Toluene	0.38	92.139	0.59	2.39	Non-polar

bond with negatively charged atoms via hydrogen bonding due to the presence of hydroxyl group (-OH group). In this instance hydrogen bonding is an important transaction because it increases the rate of TICT state formation [25]. Ethylene glycol has a slightly larger dipole moment than methanol (2.36 vs. 1.70) and this property plays an important role in determining their attraction to other atoms while also mediating dipole-dipole interactions which have the ability to increase atoms' attractions by lowering the potential energy. Toluene is a non-polar solvent with a very low dipole moment of 0.38, dielectric constant of 2.39 (dielectric constant is the measure of an atom's resistivity to a formation of an electric field) and doesn't have hydroxyl groups, thus limiting its ability to undergo hydrogen bonding. Dimethyl sulfoxide is a dipolar aprotic solvent with the highest dipole moment of 3.96 and the highest dielectric constant of 48.90 among the four chosen solvents. Dipolar aprotic solvents are unable to form hydrogen bonds due to absence of a hydroxyl group and a significant dipole moment. Since the quantum yield of molecular rotors is dependent on viscosity of its environment, the viscosity of solvents used in this study reflect a wide range of values, starting with ethylene glycol with the highests value of 16.06 mPa·s, followed by dimethyl sulfoxide at 2.47 mPa·s, while toluene and methanol are much closer in values, with toluene at 0.59 mPa·s and methanol at 0.54 mPa·s, which justifies the normalization. In some cased the curve fit is poor and delivers extreme results, as in the case of molecular rotors **1** and **3** in toluene.

It was hypothesized that the underlying mechanism for shear sensitivity of molecular rotors was their ability to polar-polar bonds through interactions with their respective solvents. In the case of molecular rotor **1**, the presence of a hyrophilic carboxylic acid as its functional group allows it to attach to alcohols (EG and MeOH). Molecular rotor **3** likewise has the same capacity to form polar-polar bonds because it has two hydroxyl groups, but unlike molecular rotor **1** which is acidic, it is alcoholic.

In polar protic solvents EG and MeOH, larger values for ΔI_{max} were seen in EG than MeOH. EG is different than MeOH in four different respects: it has higher viscosity, dipole moment, dielectric constant and molecular weight. Moreover, its values for ΔI_{norm} are much higher for all three molecular rotors, and it reaches saturation much faster for molecular rotor **1** and molecular rotor **3**, but not molecular rotor **2**, which has triethylene glycol ester for its functional group and cannot form polar-polar bonds.

Of the four solvents used, DMSO has the highest dipole moment and dielectric constant, while its viscosity is just behind EG. Since it is dipolar aprotic, it can form polar-polar bonds but cannot undergo hydrogen bonding, and in our experiments, our original assumption that polar-polar interactions are responsible for shear sensitivity proved not true. Shear sensitivity with repeatable timecourses was seen in cases of molecular rotor **2** and molecular rotor **3**, but not molecular rotor **1**.

Non-polar toluene doesn't have any free hydrogens which can be used to for polar-polar bonding, however it was found to be shear sensitive for all three of our molecular rotors. Toluene viscosity is marginally higher than methanol's, but its molecular weight is the highest among the four solvents. Very large values for ΔI_{max} were recorded for molecular rotor **1** and molecular rotor **3**, but not in the case of molecular rotor **2**. This is probably due to the ambiguity of the curve fit, since in these two cases the preferred one was the Boltzmann sigmoidal. Observations in Fig. 6.14 show the values for ΔI_{norm} as a function of molecular rotor properties: viscosity, dipole moment and dielectric constant. In each solvent we can see that values for each molecular rotor are very similar in value, but if we look at them with respect to solvents, it can be seen that in the case of DMSO which has the highest values for dipole moment and dielectric constant, its values for ΔI_{norm} are much closer to methanol, while ethylene glycol has the highest value for ΔI_{norm} in each case. This points to a contribution of solvent to fluorescence intensity.

Recent reports by Rumble et al. on the effects of fluid flow sensitivity of CCVJ and DCVJ raises some intresting questions [6]. They attribute the shear sensitivity effect of aforementioned molecular rotors in certain viscous solvents to a photoisomerization effect. Molecular rotor DCVJ has only isomer, and CCVJ has two isomers, E and Z (Figure 6.15).

In the absence of light according to Rumble et al., non-fluorescent isomer Z which has low or even zero quantum yield reverts to isomer E [6]. Stirrer experiments with CCVJ, JuliN1, and molecular rotor KE.3.61 which can not undergo isomerization, support Rumble's conclusions. Stirrer experiments with CCVJ in EG with whole-volume LED excitation light show no noticeable peak fluorescence emission shift. Intensity recovery of CCVJ in EG and in DMSO shows a markedly higher intensity increase while the solution was being stirred over a period of 7 hours, thus supporting conclusions by Rumble et al. On the other hand, in the case of molecular rotor **1** in the non-polar solvent toluene, emission intensity continued increasing even during period when no new fluid was injected into quartz tubing, as seen in Figure 6.16. To adjust for this effect, a shutter was used to block out any light which might be causing the intensity increase, and only opened when the fluid injection commenced. This finding and the noticeable intensity increase with each flow rate in non-polar solvents point to some additional influences on shear sensitivity beside isomerization.

While Rumble et al. observations are supported by our stirrer cuvette results, questions arise regarding their assumptions made about the role of solvents and whether they con-

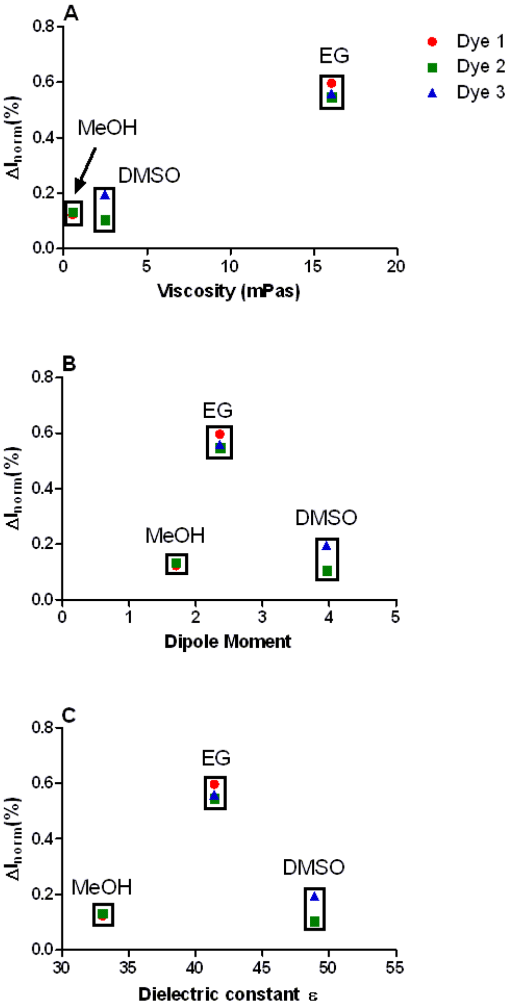

Figure 6.14: Normalized intensity response as a function of molecular rotor viscosity (A), dipole moment (B), and dielectric constant (C). Points in each group (polar protic and dipolar aprotic) are in close proximity.

tribute to intensity increase. Figure 6.17 shows an illustration of our quartz tubing used in our experiments. The cross-sectional area is ≈ 0.09 cm^2 and at the lowest flow rate of 0.25 $\frac{ml}{min}$ the fluid injected into it travels at the speed of 0.47 $\frac{mm}{s}$, and at the highest flow rate of 4 $\frac{ml}{min}$ it travels at the speed of 7.4 $\frac{mm}{s}$. The small volume that is excited and where emission

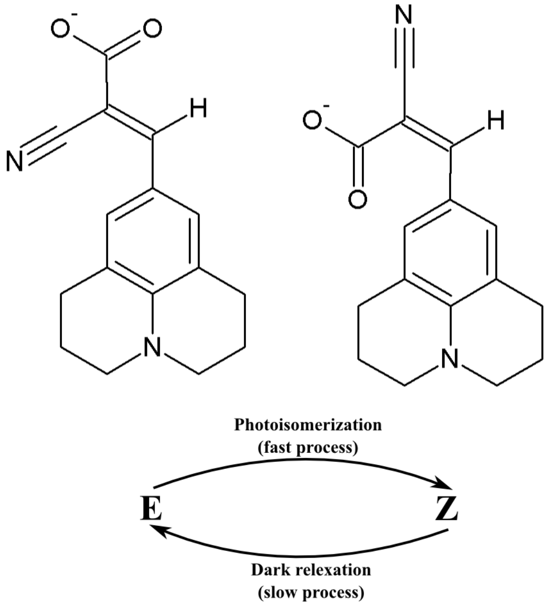

Figure 6.15: Hypothesized isomer formation of molecular rotor **1**. The head group of the is asymmetric and contains a carboxylic acid group and a nitrogen. Isomer E is converted to a non-fluorescent isomer Z during a fast photoisomerization process, while during a slow relaxation process in the absence of light, isomer Z reverts to E conformation.Adapted from [6].

is measured, is replaced very quickly. In this instance the entire volume is replaced and the new fluid injected after refilling. Rumble et al. claim that the associated intensity increase is solvent independent and is solely based on the z-isomer. They also claim that the recovery of the E isomer takes days, however in our experiments we consistently see intensity increase. Therefore, isomerization itself cannot explain the difference between the solvents and their respective intensity increases.

Our experiments were designed with the purpose of discerning additional information about molecular rotors which can help us with the understanding of their physical chemistry guiding their interactions with other atoms. We hypothesized that one of the underlying causes of shear sensitivity of molecular rotors is their ability to form polar-polar bonds. This

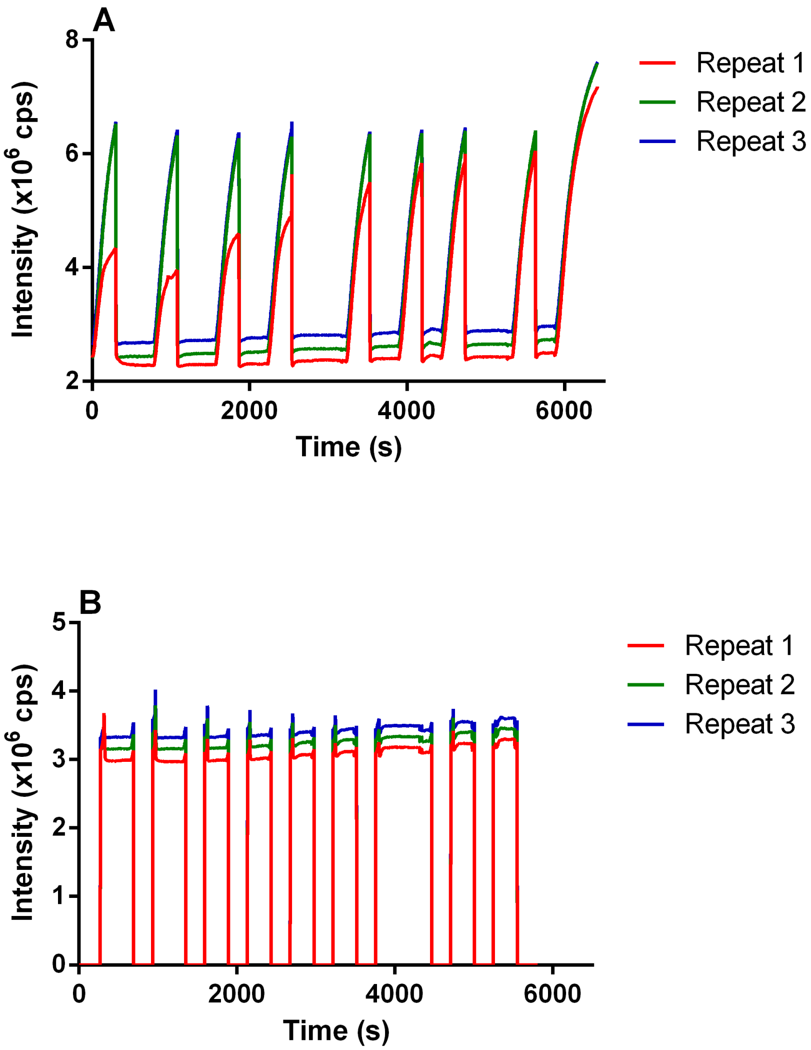

Figure 6.16: A timecourse scan of a 10 μM solution of molecular rotor **1** in toluene (N=3) without shutter(A) and with shutter(B). Shutter was applied to before and after each flow rate was applied in order to establish a steady state baseline.

was proved not to be the case, and our research, while not providing us with the definitive answer to our original question, does provide us with more information about mechanisms of molecular rotors fundamental properties, most notably the effect of their respective isomer

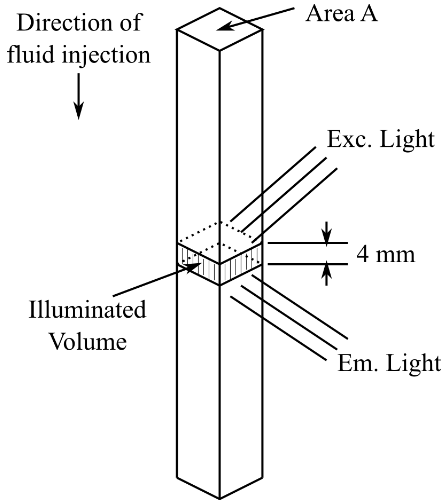

Figure 6.17: Side view of the quartz tubing used for fluid injection. Area A is ≈ 0.09 cm^2. When the fluid is injected at the flow rate of 0.25 ml/min it crosses the area A with speed of 0.47 $\frac{mm}{s}$.

formation and solvent polarity. Findings in Figure 6.14 can not be explained by assumption of Rumble et al., rather they point to a major role of solvent in either the E-Z and Z-E isomer transition, or an additional mechanism presently unknown. At this point it would be helpful to examine the fluorescence recovery of molecular rotors in different solvents over long periods of time and see how solvents effects their intrinsic properties.

Chapter 7

Applications of Fluorescent Imaging in Developing Cotton Bolls

A major pest complex (Hemiptera: Pentatomidae) commonly known as stink bugs with piercing mouthparts, are responsible for significant damage to various crop, including cotton bolls. Recently, research by in our lab has focused on this problem with a goal to improve existing methods of crop damage detection [7].

Feeding by stink bugs on cotton bolls has a detrimental role for their development and the quality of lint. Once the piercing mouthparts damage the lint, deformities and decay of healthy tissue begins, and once the lint enclosure is opened, lint quality is reduced due to staining. This has the effect of rendering it commercially unviable and can cause significant monetary damages. Contemporary methods to examine whether cotton bolls had been infested or not, include opening cotton bolls manually and looking for lesions on the lint or any discoloration. Even if this is found to be the case, the lint is damaged irretrievably. However, for those farmers tending the crops, this can be used as a sign to apply appropriate treatments. In the best case scenario, this may not be sufficient or timely enough due to the late response and the large amount of damage done. We noticed that once the stink bugs make damage to the exterior shell of the cotton bolls, they leave a unique signature, visible under UV light, and can be seen in Figure 7.1.

Figure 7.1: Images showing a cotton boll damaged by stink bugs. Yellow lesions can be seen on internal carpal wall (Panel A), yellow/brown stained regions on the lint (Panel B), and a fluorescence reflectance image of the same infested sections of the cotton boll (Panel C) [7].

Southern green stink bugs (*Nezara Viridula*(L.)) is the preponderant type of stink bugs found in the southeastern U.S.A. and the damage done to cotton bolls by its adults (Figure 1A) and small nymphs (Figure 1B) produced yellow/brown discoloration on the lint, while developing warts can be seen on interior carpal wall. Damaged regions of the lint and carpal wall exhibit blue/green fluorescence when subjected to long wavelength UV illumination. Particularly prominent are circular fluorescent spots of varying size on the interior carpal wall (Figure 1C). These spots indicate where the stink bug proboscis penetrated through the exterior wall, and piercing holes can be seen in the middle of those spots in certain cases, while in others it is absent.

An insect colony was started with 50 adult green stink bugs, and cultivated in a controlled lab and greenhouse environment. Over time, wild individuals were introduced to prevent colony from declining in potency. fifth instars of southern green stink bugs were allowed to feed on cotton bolls by keeping them encased around healthy cotton bolls (Figure 7.2). To analyze properties of healthy and damaged cotton boll tissue, a spectrofluoremeter was used. Fluorescent properties were obtained by performing a 3D matrix scan, and fluorescence intensity with respective excitation and emission wavelength was recorded.

Figure 7.2: Stink bugs in a controlled environment feeding on cotton bolls while enclosed in a meshed bag.

The 3D matrix scan of damaged cotton boll tissue is shown in Figure 7.3. The excitation wavelength ranged from 300 nm to 500 nm, with associated emission range of 320 nm to 585 nm. Two peaks can be seen: a high intensity peak A (exc=340 nm, em=430 nm), and peak B (exc=410 nm, em= 470 nm) with much lower intensity. Peak A is responsible for the blue-green fluorescence on damaged cotton bolls seen in Figure 7.1, and is approximately 3.8 times stronger than peak B. Peak C was markedly lower than peak A, but stronger than peak B and is believed to be responsible for chlorophyll emission, based on earlier reported observations.

Healthy cotton boll tissue 3D matrix scan is shown in Figure 7.4, and served as negative

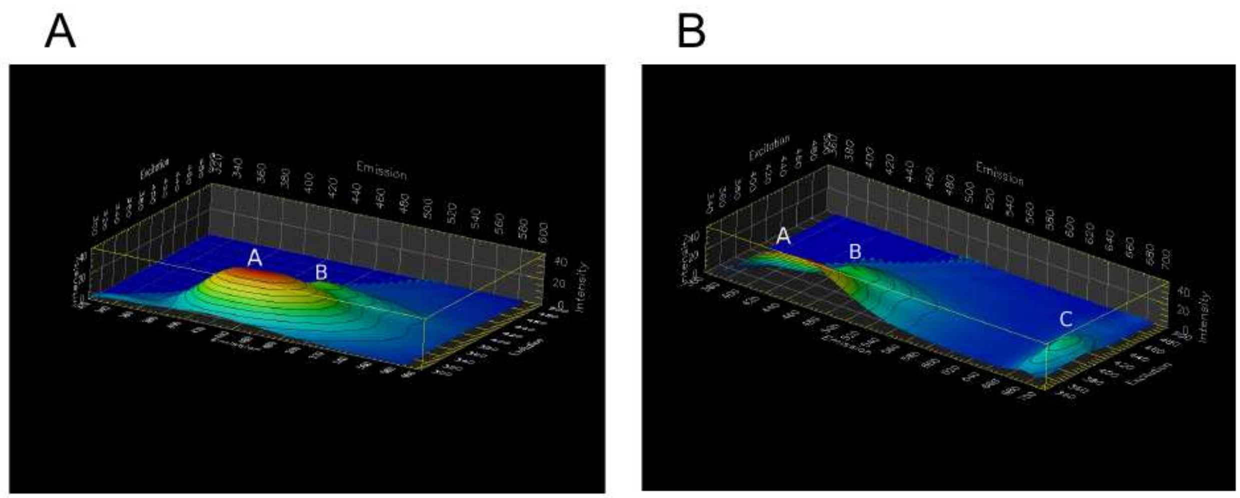

Figure 7.3: 3D graphs of matrix scans conducted on cotton boll lesions caused by stink bugs. Panel A: Emission was recorded from 320 nm to 585 nm while excitation was recorded from 300 nm to 500 nm. For the peak A excitation ranged from 320 nm to 380 nm, and emission from 380 nm to 480 nm. Peak B was excited from 380 nm to 440 nm and emission from 460 nm to 480 nm. Panel B: Emission recorded from 370 nm to 685 nm, while excitation was recorded from 350 nm to 500 nm. Peak C emitted from 660 nm to 690 nm with excitation from 380 nm to 440 nm. Fluorescent peaks A and B correspond to peaks A and B in Panel A [7].

control. The excitation ranged from 350 nm to 500 nm, with associated emission range from 370 nm to 685 nm. Peak A is about 3 times weaker than peak A in Figure 7.3, while peak B is not visible. Peak C representing chlorophyll emission is much higher than the corresponding peak in damaged cotton boll tissue.

Fluorescence spectroscopy methods have been utilized as assessments of food quality, and in combination with imaging modalities can provide a visualization method to observed physical damage in cotton bolls and other crops. Studies performed on damaged and non-damaged cotton bolls show how stink bug feeding produces a unique blue-green fluorescence under UV light. In regions of cotton bolls damaged by stink bugs, chlorophyll is diminished, and when opened additional damage can be seen on the lint and inner carpal wall. This novel

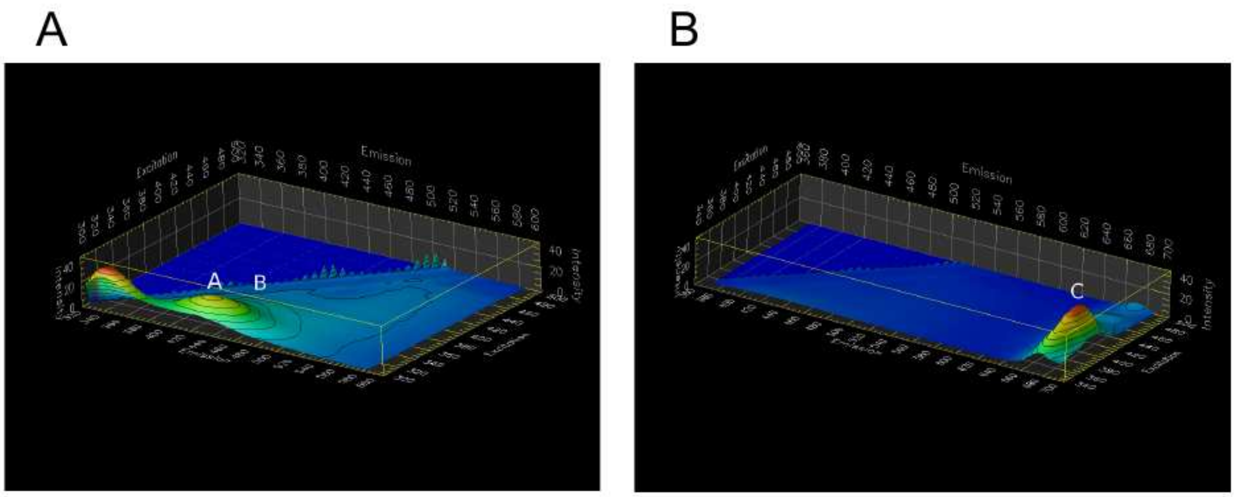

Figure 7.4: 3D graphs of matrix scans of non-infested cotton boll tissue. Panel A: Excitation ranged from 300 nm to 500 nm with emission from 320 nm to 585 nm. Peak A was excited from 300 nm to 320 nm and it emitted from 320 to 360 nm. Panel B: Excitation ranged from 350 nm to 500 nm with emission from 370 nm to 685 nm. Peaks A and B from panel A are excluded from Panel B since their corresponding excitation range wasn't included. Peak C represents chlorophyll with excitation from 380 nm to 430 nm and emission from 660 nm to 690 nm [7].

method of fluorescent imaging has a chance to become an efficient way to detect damage and optimize stink bug prevention.

Chapter 8

LED-Induced Fluorescence and Image Analysis to Detect Stink Bug Damage in Cotton Bolls

8.1 Background

The southern green stink bug (*Nezara viridula* L.) (Hemiptera: Pentatomidae) is one example of a stink bug that feeds on and thereby damages plants. This species is thought to be originally from Ethiopia, but is now found in many tropical and subtropical regions of the world. This species is commonly found in the southern United States where it is considered a major pest attacking agricultural crops. All stink bugs feed on a variety of wild and cultivated plants and crops including but not limited to legumes, nuts, and various fruits and vegetables [26–29]. One of the extensively planted crops in the southeastern U.S. susceptible to stink bug infestation is cotton (*Gossypium hirsutum* L.) [26]. Most stink bugs feed on developing cotton bolls, which occur after anthesis. Both nymphs and adults are capable of feeding and damaging crops. Mature nymphs tend to cause more damage than younger instars [30].

The feeding mechanism of stink bugs includes the extension of a piercing mouthparts (proboscis) with which it penetrates the outer wall through which the mouthparts are extended to reach developing seeds. Pathogenic bacteria may be introduced during feeding thereby adding an additional destructive agent resulting in further degradation of bolls, especially the less mature ones [31, 32]. Cotton seeds damaged by stink bugs result in greatly reduced fiber length, quality, and uniformity. [33–35]. Another effect of stink bug feeding on cotton bolls is the lower rate of seed germination [36]. These types of damage greatly diminish the value of cotton lint and can cause substantial impediments to a stable cotton supply.

A method to reduce the number of pests present in cotton boll fields is to use cover crops like clover and different types of legumes as breeding grounds where pests could achieve maturity and be kept away from cotton [37]. However, by far the most common approach is to wait until damage exceeds an economic threshold and then apply insecticides to mitigate the population.

While highly specific insecticides and genetic engineering of the host crop have become preponderant methods in agricultural pest control, these methods have not been effective against stink bugs. Therefore, stink bugs are generally managed using broad spectrum insecticides, such as pyrethroids and organophosphates, that kill the intended pests but also many non-target beneficial insects. Proper timing and application of insecticides is critical to reduce the risk of secondary pest outbreaks [38, 39]. To prevent financial losses, insecticides need to be applied only when the estimated damage exceeds an economic threshold.

Moreover, the choice of insecticide chemistry can have a profound effect on efficacy and price. Along with choosing appropriate types of insecticides for application, timing is important because organophosphates and pyrethroids have very limited residual activity in the field. In other words, insecticides need to only be applied at the correct time and place or the grower risks erosion of financial gains.

To develop an appropriate plan for pest control in the field, two requisite and codependent challenges regarding sampling and damage detection are necessary. The currently recommended practice to cotton boll sampling is time consuming, burdensome, and destructive to the test population of cotton bolls. Recent studies describe various issues with monitoring stink bug populations which are predisposed to aggregate in fields and can be difficult to detect with the naked eye [40, 41]. Even with optimized sampling plans, cotton boll examination for potential damage is an invasive procedure which renders the bolls useless because it requires them to be cracked open. Development of a new method with proven accuracy and efficiency to detect stink bug feeding is necessary.

Presently, new methods to detect stink bug presence and damage to cotton bolls are being developed. These methods involve the use of an electronic nose as a sensing device to determine if chemicals emitted by stink bugs or damaged plants can be detected [42]. Tests conducted under lab and field conditions show promising results [43]. It is of essential importance to continue research in this field because of the economic importance of cotton. Currently the U.S.A. is the world's dominant cotton exporter, with cotton stocks expected to increase to more than 16 million bales by 2019, representing about 35% of the global trade [44].

In this article, we propose an image analysis technique that builds on previous research by our lab [7]: the presence of different fluorescence emission was reported, depending on whether the cotton boll was damaged by stink bugs or not. Stink bug feeding results in a unique fluorescent signature on the cotton boll wall that can be imaged and analyzed for discriminating properties. One of the advantages of this technique is that it is non-invasive and nondestructive. Here, we report on an image segmentation and analysis process capable of distinguishing feeding marks from stink bugs versus those caused by other factors.

8.2 Methods

8.2.1 Stink Bug rearing

Southern green stink bugs were reared in the laboratory on a diet of fresh green beans or okra pods following the methods of Harris and Todd [45]. Briefly, adult stink bugs captured in the field were brought into the lab and placed in 37.9 liter glass aquaria lined with paper towels. Adults oviposited on the paper towels which were transferred to ventilated petri dishes until the eggs hatched and then maintained in petri dishes or small plastic wide-mouth jars at 25.0 C and 65% relative humidity. Adults used for infesting bolls were less than two weeks old and of mixed sex.

Cotton plants were started from seed and grown in the greenhouse to produce bolls for the study. Three cotton seeds (FM 9063 B2RF) per 11.35 liter plastic pot were sewn per in Metro Mix 300 growing medium. After germination, two of the plants were culled and the remaining plant was fertilized monthly with Osmocote 14-14-14 and Micromax fertilizer (the Scotts Co. LLC, Marsville, OH). Once the plant began flowering, individual white flowers were marked daily using flagging tape and then allowed to develop normally for 10 to 14 days. When the bolls reached 10 to 14 d past anthesis, a single southern green stink bug adult was caged in a mesh bag on each boll and subtending leaf for a period of 48 h. After treatment with the stink bug, bolls were excised from the plant and shipped with overnight service to the Athens campus for imaging. At the time the bolls were cut from the plant they had an external boll diameter of 2.3 to 2.5 cm. Control bolls were treated exactly as described, except that no stink bugs were introduced into the mesh bags. A total of 136 bolls were harvested that were exposed to a stink bug, and 109 control cotton bolls were harvested.

8.2.2 Mechanically Punctured Cotton Bolls

Sixteen cotton bolls were punctured with a sterile syringe needle (31 Ga, 8mm long, Beckton-Dickinson, product no. 328418) as a control. These bolls were treated exactly as described in the previous section, except that no stink bugs were introduced into the mesh bag. Before harvesting, the bolls were gently cleaned using rubbing alcohol on a cotton swab to remove any microorganisms that could contaminate the boll. Puncturing was done manually, and care was taken that the needle penetrated into the lint tissue. The punctured bolls were harvested immediately. Bolls with needle punctures were processed in the same manner as the other bolls. The purpose of these controls were to examine the difference between purely mechanical puncture damage and the specific puncture damage caused by stink bugs.

8.2.3 Imaging Apparatus

The imaging apparatus, shown in Figure 8.1, consisted of a consumer-grade digital single lens reflex (SLR) digital camera (Konica Minolta, Dynax Maxxum 7D, Tokyo, Japan) with a Sigma 50 mm f/2.8 fixed focus lens. An emission longpass filter (490nm, Chroma Technology Corp., Brattleboro, VT) was positioned on a post in front of the camera. Two LED sources (Philips/Luxeon LXHL-LR5C) with custom LED driver provided a continuous and homogeneous excitation light at 440 ± 20nm. Additional excitation bandpass filters D450/40 (Chroma) were placed on the LEDs to reduce the spectral overlap between excitation and emission light. A rotary stage held cotton bolls during imaging, and the non-fluorescent black cardboard behind reduced background fluorescence and scattered light.

Image acquisition and processing

All images were acquired with lens aperture set at f/11 and an exposure time of 15 seconds. All automatic camera functions were disabled, the white balance was fixed to 5500 K, camera

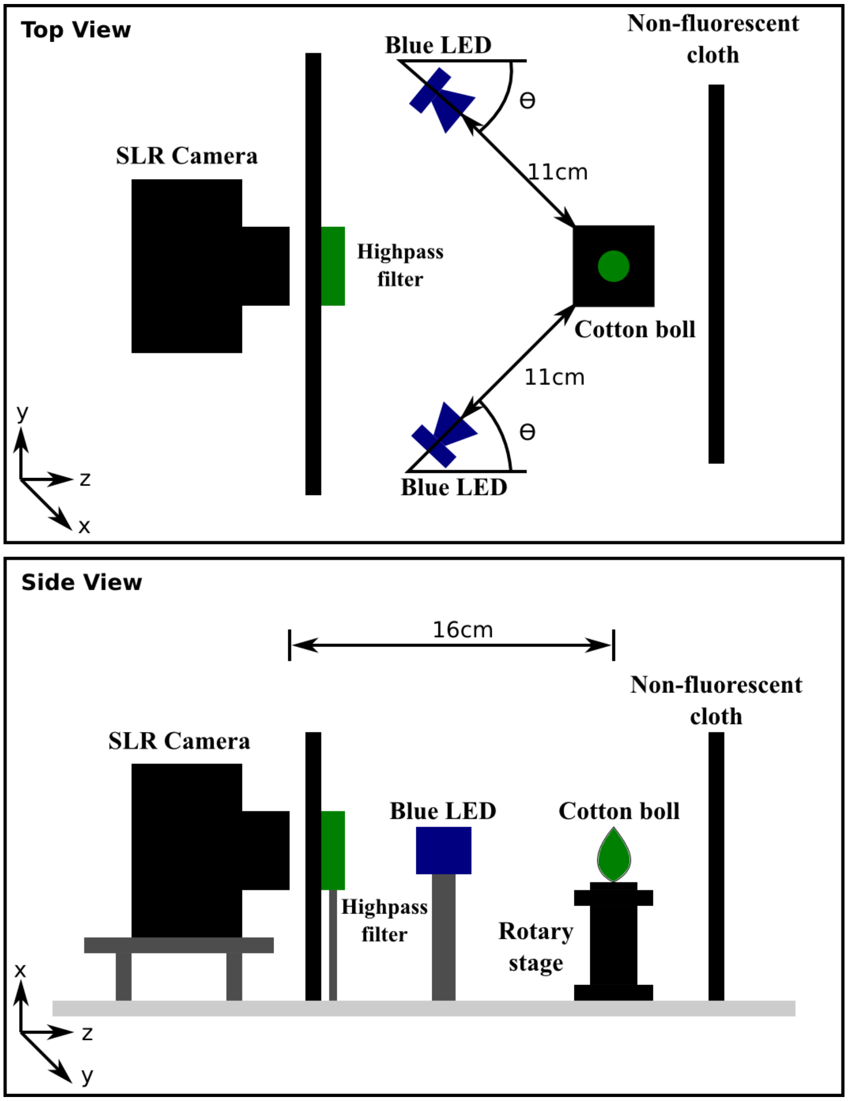

Figure 8.1: Top and Side view of the imaging apparatus. A SLR camera is mounted on posts in front of the sample, with an dichroic emission longpass filter placed between sample and lens. Two blue LED sources at θ=45° angle from the lens-sample path) provide a homogeneous excitation light. The cotton boll sample is placed on a rotary stage to allow images taken from all sides. A non-fluorescent black cloth backdrop blocks scattered light and background fluorescence.

sensitivity kept at ISO 400, and the camera set to acquire raw images in MRW (Minolta Raw) format. Each cotton boll was placed on the rotary stage and rotated 90° after each image acquisition, resulting in four images per cotton boll. Raw-format images have a depth of 12 bits per pixel, and all images were converted with UF-Raw (http://ufraw.sourceforge.net) to 16-bit TIFF images with the 12-bit depth fully retained.

All further image processing was performed with Crystal Image [46], a quantitative image analysis software. The images were first subjected to a center-weighted median filter, and their resolution reduced to 1508 by 1004 pixels with a 2x2 binning operation. The reduced-scale images showed a resolution of 18 pixels/mm. After the initial steps, two different paths were taken: Mask creation, and computation of a ratiometric image. For the mask, the red channel was blurred with a second-order Butterworth lowpass filter with a cutoff of 10 pixels^{-1}.

Background separation was performed with a fixed threshold, made possible by the black cloth backdrop. The resulting mask contained the image value 1 for all pixels that correspond to the cotton boll, and 0 for all background pixels. The ratiometric image was computed by extracting the red and green channels from the RGB image and dividing the green channel by the red channel on a pixel-by-pixel basis. Subsequent multiplication of this intermediate image with the mask, also on a pixel-by-pixel basis, yielded an image that contained zero-valued pixels for the background and the green/red intensity ratio for the cotton boll pixels. The image processing steps are illustrated in Figure 8.2.

Candidates for stink bug puncture marks were identified with a local maximum filter with the *a priori* settings of a peak-to-peak distance of 15 or more pixels and a minimum intensity difference of 10 to the average inside a 15-pixel radius and segmented with a variant of the greedy snake algorithm [46]. Fluorescent marks were excluded from analysis when their area was below 28 pixels (0.09 mm^2) or their integrated intensity was below 0.04 mm^{-2}. Furthermore, all fluorescent marks with an aspect ratio greater than two or with a convex shape were excluded. The snake was then converted into a circle, and the average intensity I_2 was measured inside this circle. A smaller concentric circular region with a radius of 4

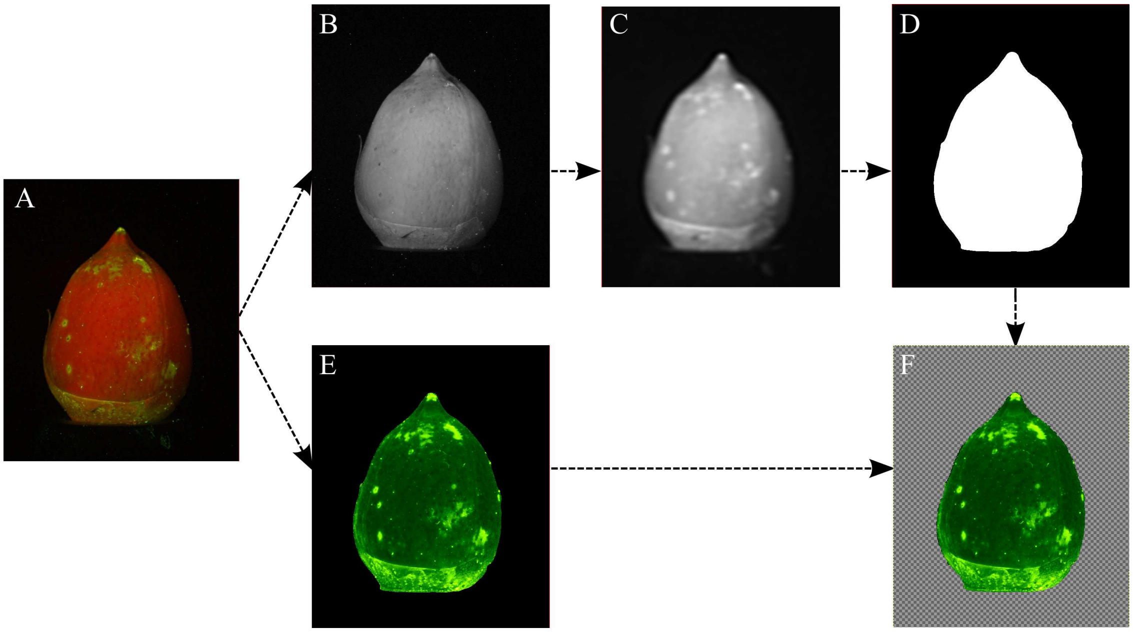

Figure 8.2: Processing steps of cotton boll images. A native camera raw image (A) is separated into the monochromatic R, G, and B channels, and the B channel is discarded. To obtain the cotton boll mask, the green channel is filtered and reduced in size (B), then further blurred with a Butterworth lowpass filter (C). The mask is then obtained by thresholding (D). In parallel, a normalized intensity s generated by dividing the green channel by the red channel on a pixel-by-pixel basis (E). Multiplication with the mask yields the final image of normalized green intensity from the cotton boll, separated from background (F). The background in (F) is indicated by the gray checkerboard pattern and is excluded from any image analysis steps.

pixels (≈ 0.05 mm^2) was then selected to compute the central average intensity I_1. A ratio I_1/I_2 was computed for each candidate for stink bug puncture marks (Figure 8.3).

8.2.4 Statistical Analysis

Statistical analysis was performed in R (http://www.r-project.org). The ability of the area metric and the intensity metric to distinguish true and false positives was tested individually with the Kruskal-Wallis test and Dunn's multiple comparison test. The choice of the Kruskal-

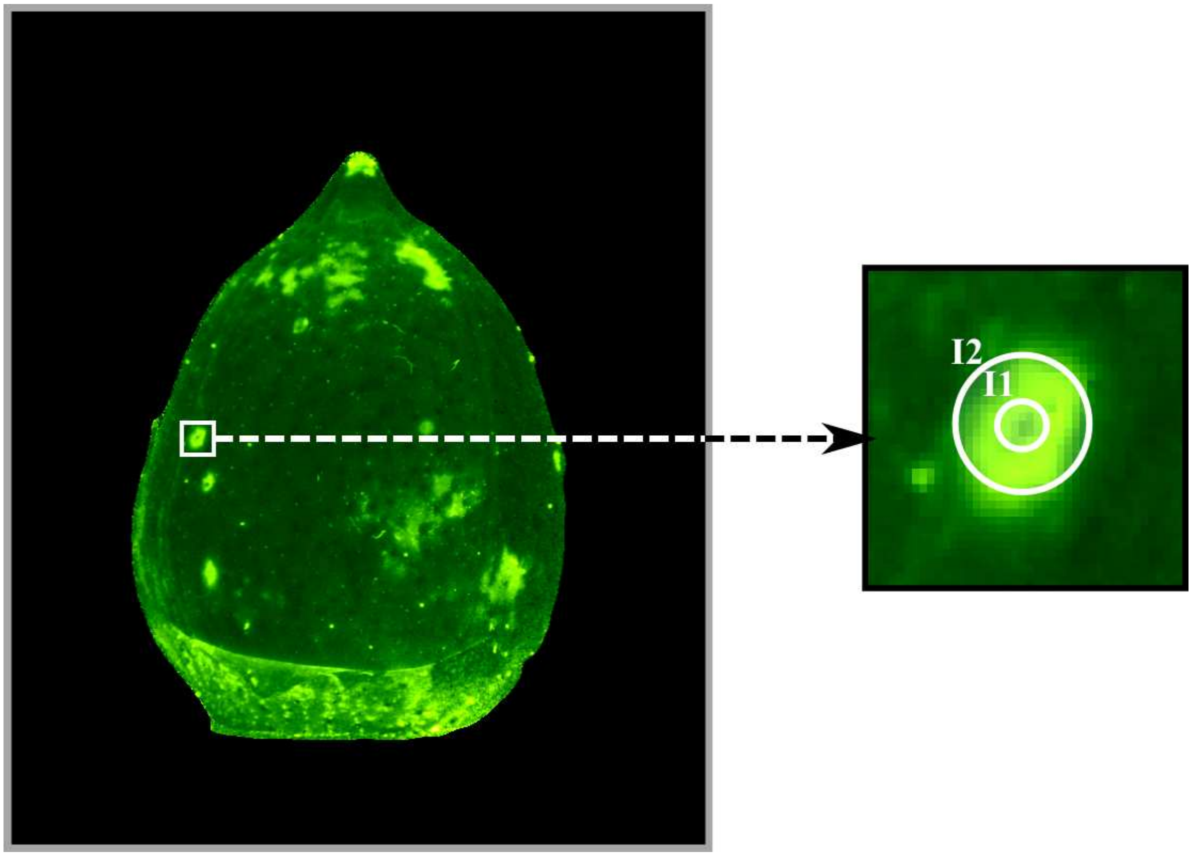

Figure 8.3: An example of how fluorescent surface damage marks on cotton bolls were selected and evaluated for analysis. Strongly fluorescent regions, identified with a local maxima filter, were analyzed with respect to area and intensity. One representative region has been magnified, and the two auxiliary circular regions indicated. Average intensity inside the smaller circle is denoted I_1, and average intensity inside the larger circle is denoted I_2. In instances where stink bugs or syringe needles made the puncture, the ratio of I_1/I_2 often falls below 1. On the other hand, when damage marks were found on non-infested cotton bolls, the ratio of I_1/I_2 was less than 1 in only 24 % of cases.

Wallis test over one-way ANOVA was dictated by the nonparametric distribution of the data. Deviation of a sample's median value from a hypothetical value was tested with the Wilcoxon signed rank sum test. A significance level of α=0.05 was assumed.

8.3 Results and Discussion

In an earlier publication [7], we reported on the observation of a characteristic green fluorescence emission near stink bug puncture sites. This fluorescence was visible with the unaided eye under ultraviolet illumination on the lint and the inner carpal wall. We also observed that some fluorescence becomes visible on the outer carpal wall, while at the same time the red chlorophyll emission recedes. Further examination of this phenomenon revealed that the stink bug marks become more prominent under deep blue excitation than under ultraviolet excitation, and further image acquisition was performed with LED excitation at 440nm. The fluorescence emission that accompanies typical damage on the inside of a cotton boll is shown in Figure 8.4. Once damaged by a stink bug, the lint starts to develop a brown color and degrade, thus beginning a process which renders it commercially unviable.

Furthermore, damaged cotton bolls that were kept in ventilated containers for several weeks started to crack open, revealing dried and degraded lint and the development of mold. A control set of bolls that were not exposed to stink bugs showed markedly less degradation, with most of them being in the same condition they were originally received in.

The purpose of this study was to provide proof-of-principle that LED-induced fluorescence combined with image analysis can provide an indicator whether a cotton boll has been fed on or not. The image processing method was developed based on the observation that (a) puncture marks cause a circular limited region to develop green fluorescence, and (b) the center of the region, where the plant tissue was removed by the puncture, actually exhibited very low fluorescence, leading to a donut-shaped intensity pattern. Examples of the image patterns are shown in Figure 8.5, both under normal fluorescence and after processing to yield the ratiometric image.

One challenge for the image analysis method is the presence of fluorescent regions that are not related to stink bug feeding (Figure 8.5 E and F). In fact, out of 109 cotton bolls that

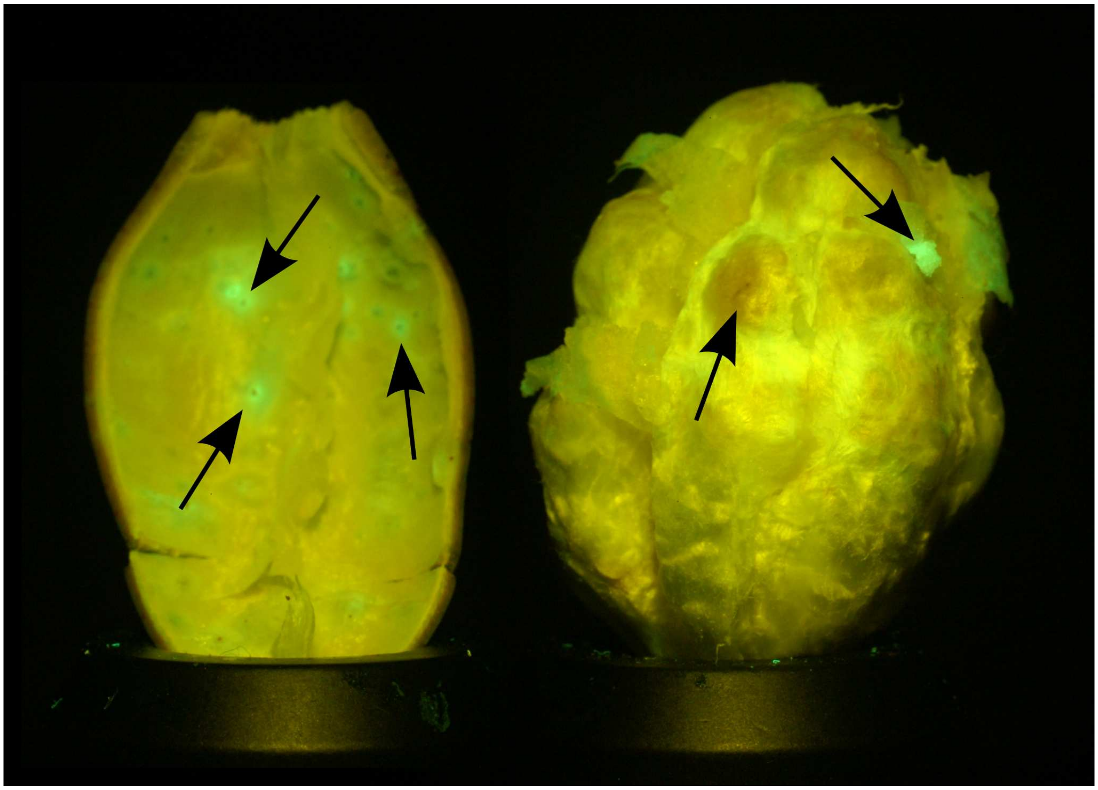

Figure 8.4: A fluorescent image of the cotton boll carpal wall (left) and cotton boll lint (right) with arrows denoting the damage caused by stink bugs. The carpal wall shows fluorescent interior warts, which often have a noticeable dark center where the stink bug pierced the wall. Stink bug damage to the lint is visible in two different ways: lint browning (visible under regular white illumination) and fluorescent damaged regions that correspond with the piercing marks on the carpal wall.

were not exposed to stink bugs, 41 showed fluorescent marks, and a total of 49 fluorescent marks met the inclusion criteria and were included in the analysis. Conversely, out of 136 cotton bolls that were exposed to stink bugs, 38 did not show any fluorescent marks, and manual examination of the inner carpal wall and lint confirmed that these bolls had not been fed upon by the stink bugs. Of the remaining 98 cotton bolls that exhibited fluorescent marks, a total of 169 marks were included in the analysis. Manual examination of cotton bolls not included in this study led to the inclusion criteria, namely, a minimum area, a minimum average intensity, and a strictly convex shape. It is conceivable that small marks are caused by non-piercing insects, such as spider mites, and large, elongated marks are the consequence of mechanical abrasion.

Clearly, any image analysis method must detect false-positive fluorescent marks. The first step of the image analysis chain was aimed at detecting all fluorescent marks, irrespective of their origin. Local maximum detection combined with either gradient-based segmentation (e.g., the hill-climbing algorithm [47] or active contours, i.e., snakes [46] or intensity-based segmentation, such as region-growing, can be used in a straightforward manner to provide the initial set of candidates. Based on the initial set of cotton bolls, we defined all fluorescent marks that were found on the control group of cotton bolls as false-positives, and all fluorescent marks that were found on the exposed group of cotton bolls as true positives. The fluorescent marks associated with needle punctures (total of 81 marks) were examined as a separate group.

The second step of the image analysis process, which was the focus of this study, was

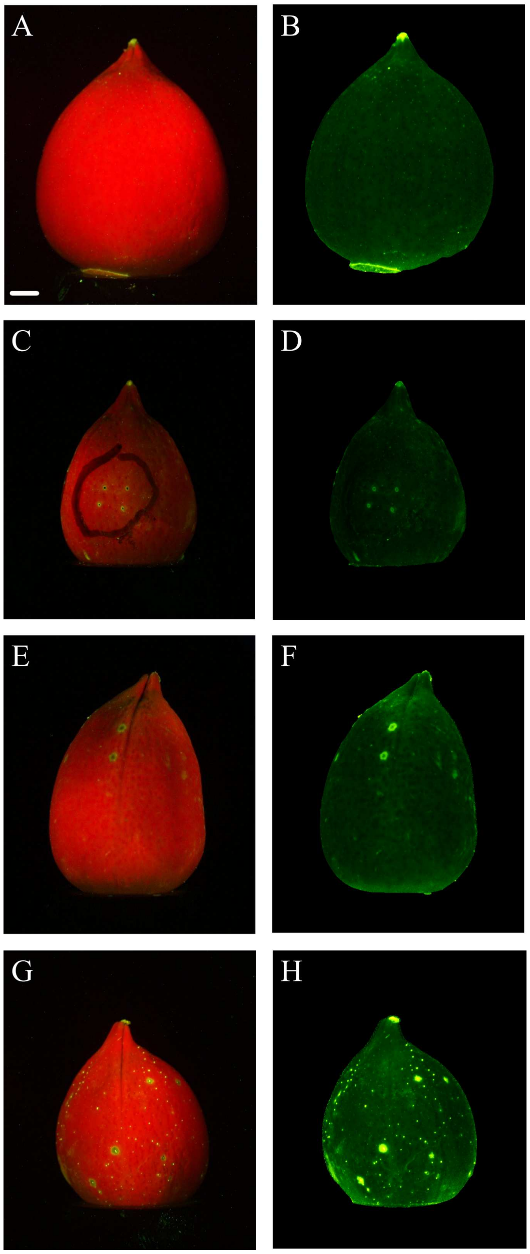

Figure 8.5: Raw color images (left column) and corresponding ratiometric images (right column) of cotton bolls with various types of damage and stages of infestation. (A) and (B) show a non-infested cotton boll without any exterior damage marks. (C) and (D) show a cotton boll punctured by a sterilized syringe for negative control studies. The black ring in (C) was drawn with a fiber tip marker. (E) and (F) represent a non-infested cotton boll with exterior fluorescent marks visible. (G) and (H) are images of an infested cotton boll with exterior puncture marks visible as larger fluorescent green regions. Note the presence of smaller auto-fluorescent dots not caused by stink bugs. The scale bar (white line in lower left corner of image A) represents 5 mm.

aimed at separating true positives from false positives. Among several quantitative metrics, size had a strong ability to separate false and true positives as shown in Figure 8.6. The median area of the fluorescent region associated with stink bug feeding was 0.35mm^2 compared to a median area of 0.6mm^2 for the false positives. The difference was statistically significant ($P < 0.0001$). Needle puncture marks caused an even smaller fluorescent region with a median area of 0.27mm^2. Size variation was less within the marks caused by stink bug feeding and those caused by the needle puncture, whereas a large variability in size was observed in the false-positive group. Median size was not statistically different between stink bug-related marks and needle puncture marks.

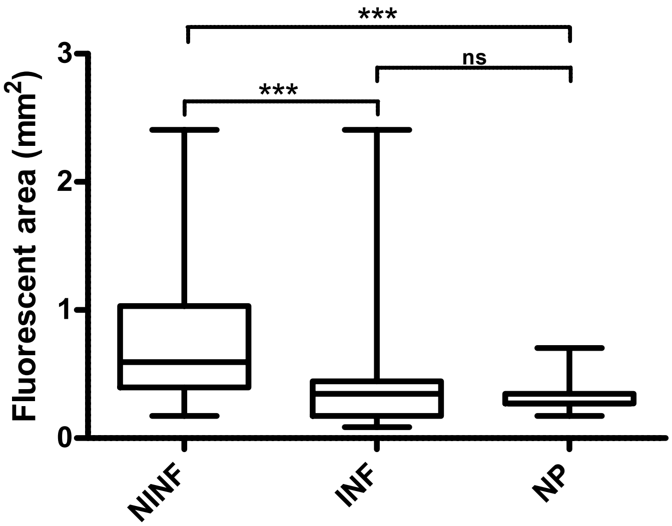

Figure 8.6: Boxplot of the area A of the segmented fluorescent region for three categories of fluorescent spots: non-infested (NINF), infested (INF), and needle punctures (NP). Median area is significantly larger ($P < 0.0001$) for fluorescent areas that are neither stink bug-related nor caused by needle puncture, but the area is not significantly different between stink bug feeding marks and needle punctures (Kruskal-Wallis test with Dunn's multiple-comparison post-test).

A second quantitative metric was obtained by measuring the intensity drop-off towards the center of the puncture mark. False-positive marks tend to have an irregular intensity distribution with the highest intensity near the center. Conversely, plant tissue that was directly damaged by the puncture was almost black under visible-light examination, and its corresponding fluorescent emission lower. It can therefore be expected that an intensity ratio of the center intensity I_1, relative to the average intensity of the entire fluorescent spot I_2, tends to be less than 1 for true-positives and greater than 1 for false-positives. A box plot of the intensity ratio can be seen in Figure 8.7. Median ratiometric intensity of the false-positive fluorescent regions was 1.2, with a statistically significant difference from 1 (Wilcoxon signed rank test, $P < 0.0001$). Conversely, median ratiometric intensity of those fluorescent regions associated with stink bug damage was 0.96, statistically significant lower than 1 (Wilcoxon signed rank test, $P < 0.0001$). For comparison, needle punctures exhibited a median ratiometric intensity of 0.86, lower than 1 with $P = 0.0002$. Similar to size, the ratiometric intensity was significantly different between false positives and true positives ($P < 0.0001$) and between false positives and needle puncture marks ($P < 0.0001$).It is interesting to note the relative similarity between fluorescent marks caused by stink bug feeding and those caused by needle puncture, which is consistent with our earlier publication [7], where we hypothesized that the fluorescence emission is the by-product of the plant healing process.

Although both the size metric and the intensity ratio metric are different between stink bug feeding marks and unrelated fluorescent spots from a statistical perspective, considerable overlap between the values of the true positive and false positive groups exists. We therefore examined if a two-dimensional separation can further improve the separation of false and true positives. A scatter plot of both groups in two dimensions is shown in Figure 8.8. Overlap still exists, but it can be envisioned that a rectangle that separates the lower left corner from the rest of the region can capture most of the true positives. Such a rectangle could, for example, combine the conditions $I_1/I_2 < 1.2$ and $A < 0.6$.

Puncture marks from infested cotton bolls have a ratio $I_1/I_2 < 1$ in 69% of the cases,

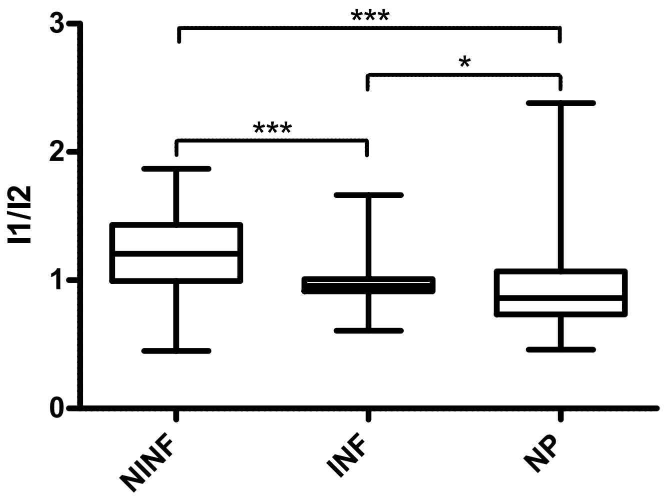

Figure 8.7: Boxplot of the intensity ratio I_1/I_2 for three categories of fluorescent spots: non-infested (NINF), infested (INF), and needle punctures (NP). Fluorescent marks that are not related to a puncture generally have a higher intensity near the center. Correspondingly, the ratio I_1/I_2 is greater than 1 (statistically significant, Wilcoxon signed rank test, $P < 0.0001$). Puncture marks tend to have a darker center, and the ratio I_1/I_2 is less than 1. This difference is also statistically significant for stink bug feeding marks and needle punctures. Furthermore, the ratio I_1/I_2 is significantly higher for fluorescent marks that are not related to a puncture than for those related to stink bug feeding and those related to needle punctures (both $P < 0.0001$ by the Kruskal-Wallis test with Dunn's multiple-comparison post-test).

whereas for false-positive damage the ratio falls below one in only 24% of the cases. Only four (8%) false-positives lie within the rectangle arbitrarily defined above, and 147 true-positives (87%) lie within the same rectangle. Contingency tables for the criteria cited above are provided in Table 8.1. Clearly, two-dimensional separation markedly improves the specificity of the detection method.

In an attempt to determine the limits of separation between true and false positives, a receiver operating characteristic (ROC) analysis was performed by increasing the size of the rectangle along a diagonal through the origin and the point (0.6, 1.2). As shown in Figure

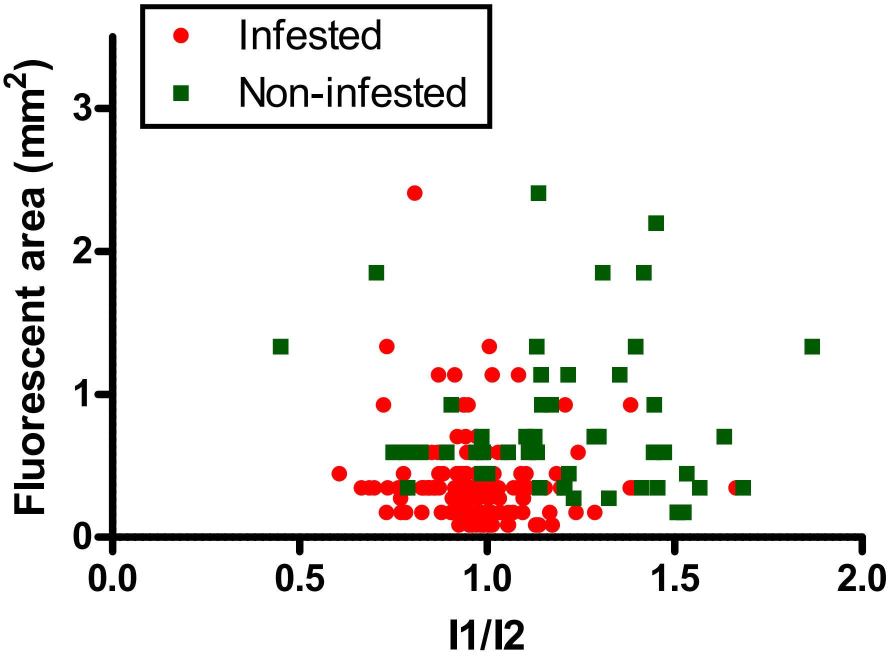

Figure 8.8: Scatterplot of all examined marks (except the needle puncture controls) arranged in two dimensions by area A and intensity ratio I_1/I_2. A multiple-threshold criterion, for example $I_1/I_2 < 1.2$ and $A < 0.6$, improves the separation of false-positive marks from true-positive marks: 87% of the true-positive marks lie inside the rectangle limited by the values of area and intensity ratio, whereas only 8% of the false-positives fall into the same rectangular region.

8.9, choice of a very small rectangle leads to high sensitivity, but poor specificity due to the exclusion of many true positives. Too large a rectangle leads to poor sensitivity due to the inclusion of the false positives. The ROC curve, however is very different from the diagonal (i.e., assumption of random data). The ROC analysis does not take into account that different separation boundaries (e.g., a diagonal line connecting $A = 1.1$ and $I_1/I_2 = 1.5$, or an ellipse) can improve both sensitivity and specificity even further. These considerations are not appropriate for this stage of the research, however, because a larger-scale study is necessary to identify data obtained in the field. It is conceivable that clustering algorithms

Table 8.1: Contingency tables for separation of fluorescent marks by their area A, their intensity ratio I_1/I_2, and both criteria simultaneously. The use of two criteria simultaneously notably increases specificity.

	$A < 0.6$	$A \geq 0.6$	$\frac{I_2}{I_1} < 1.2$	$\frac{I_2}{I_1} \geq 1.2$	$A < 0.6$ and $\frac{I_2}{I_1} < 1.2$	$A \geq 0.6$ or $\frac{I_2}{I_1} \geq 1.2$
Infested	153	16	161	8	146	23
Control	27	22	24	25	13	36

can provide the boundary from a training data set, and points placed in the two-dimensional coordinate system can be assigned to their respective cluster. For practical purposes, an 87% detection of true positives with only 8% false-positives is already acceptable when we consider that the main goal of the application of this method in the field is the approximate determination of the level of stink bug infestation.

8.4 Conclusions

Among the many challenges facing agronomists in growing cotton, two stand prominently: detection of internal damage and determination of its underlying cause. With respect to cotton, current methods include harvesting immature cotton bolls and opening them so any damage can be visualized. Even if no damage is observed, the cotton bolls are lost irretrievably due to destructive sampling. Challenges arising from this method includes the way the observations are made. Once the cotton boll is opened, it is hard to visualize stink bug damage unless the degradation has already started and the disease process is well underway. Even then, application of pesticides could be already late. In other words, if a grower couldn't detect damage very soon after it occurred, the bugs may have moved and insecticide application would not yield any economic benefits.

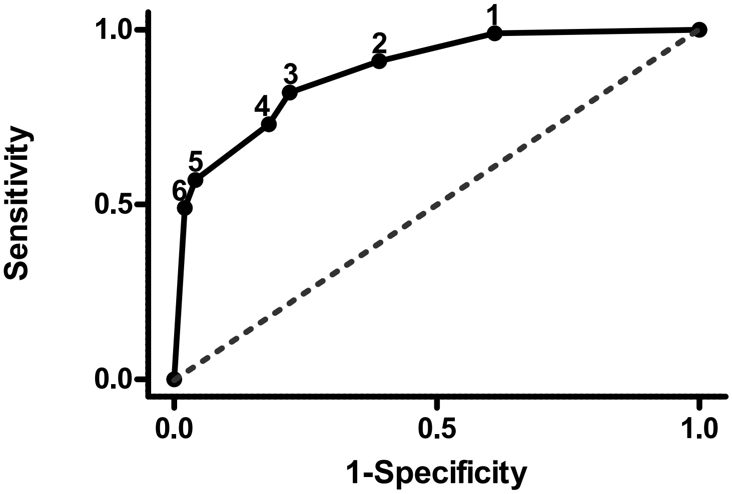

Figure 8.9: Receiver operating characteristic (ROC) for different-size rectangles (*cf.* Figure 8.8) as a study how well a dual threshold criterion can separate true and false positive fluorescent marks. As specific corner points for the rectangle in Figure 8.8 were chosen: 1: (1.5, 1.4), 2: (1.0, 1.2), 3: (0.8, 1.1), 4: (0.65, 1.05), 5: (0.5, 1.0), 6: (0.4, 0.98). At point 1, sensitivity is high but specificity is low, and this changes towards the higher point number. At point 6 we reach lower values for sensitivity but higher values for specificity. Striking a balance in this instance includes reducing the number of false positives (high sensitivity) and false negatives (high specificity).Dashed line represents a random assumption.

To overcome these limitations, we present one step towards a field applicable imaging method to estimate the levels of stink bug infestation. In our previous work, we identified a fluorescent wand and a fluorescent image scanner as possible devices to detect stink bug-related fluorescence. Further analysis of the fluorescent marks, as presented in this study, reveals that the wand is likely impractical due to the presence of a large number of false-positive fluorescent marks. The second device that we proposed is a light-shielded enclosure in which fluorescence emission can be detected by pushing the cotton boll into the enclosure. With a suitably engineered device, the cotton boll might even be left on the plant. The next step of this project is the engineering design of an imaging scanner that can be used in the field.

Chapter 9

Unsupervised Image Analysis Template to Detect Damaged Cotton Bolls

9.1 Introduction

Green stink bugs (*Nezara Viridula* L.) from Hemiptera: Pentatomidae is a invasive and destructive agricultural pest found in North America. Though to have originated in eastern Africa, it is nowadays found on several continents where it is responsible for significant damages to a wide variety of plant sand crops, including but not limited to fruits, vegetables, and especially in the southeastern U.S.A., cotton (*Gossypium hirsutum* L.) [26].

During the blooming stage when the cotton bolls are most susceptible to physical damage, green stink bugs (mostly from higher developmental stages, but also younger nymphs) begin infestation. Green stink bugs pierce through the outer wall of cotton bolls with a needlelike mouthpart called proboscis, which when extended, can pierce all the way into the developing lint. The consequences of this process are mainly twofold: reduction in new seed germination rate, and diminished lint quality [31].

A fluorescent image of a cotton boll subjected to stink bug infestation is shown in Figure 9.1. Green fluorescent warts are visible on the inner carpal wall where the stink bug proboscis punctured it, and on the lint smaller fluorescent regions can also be see. The lint has started to go through a gradual process of degradation with early indications of lint browning visible. This process is irreversible, and once started ultimately ends in the destruction of the lint

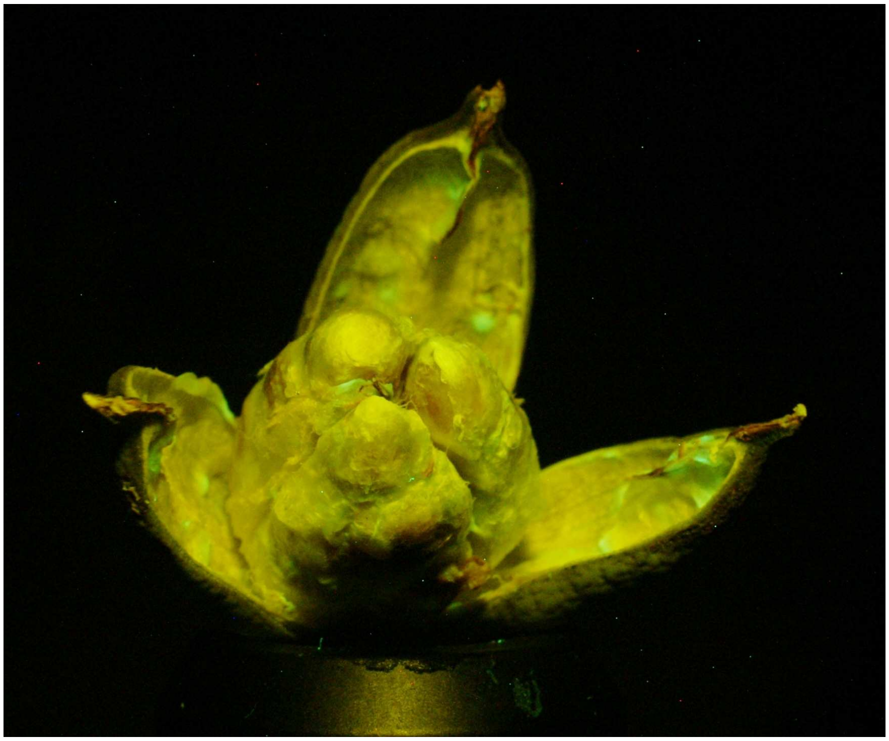

Figure 9.1: A fluorescent image of a damaged cotton boll showing damage made by stink bugs. Fluorescent regions on the carpal wall are warts caused by the stink bug proboscis puncture, penetrating all the way into the ling, and starting its discoloration.

Any damage to lint is potentially devastating, since it results in discoloration, and reduction in fiber strength and consistency. In the aftermath, what is left is a damaged crop with almost non-existent market value. Current methods to control stink bug populations is to apply insecticides and hopefully prevent infestation from spreading.

While modern techniques like genetic engineering and advances in insecticide development targeting specific insects have become preponderant methods to control and contain stink bug infestation, their effectiveness in cotton fields hasn't reached optimal point due to several factors. The most important factor concerns the proper timing and application of insecticides with respect to the populations size [38,39]. Since the cost of pest control shouldn't exceed the inherent market value of the crop under cultivation in real value terms, the choices made by cultivators by definition represent limiting factors determining their effectiveness. Insecticides need to be applied in a timely manner before large groups of stink bugs are able to cause damage. Moreover, the choice of insecticides matters significantly, since they can be customized to target stink bugs in different development stages in which they cause most damage more adequately. Along with choosing appropriate types of insecticides for application, the timing when it is applied can reduce its potency, because insecticides typically have limited durability which decays over time. If insecticides are sprayed in sufficient quantities but at an inopportune time when the stink bugs traveling in large groups had already caused extensive deterioration in cotton bolls' condition, or if stink bugs arrive after the potency of insecticides had greatly decayed, then the underlying conditions regulating the infestation prevention can change adversely. These concerns can be cogently reduced if a method to identify the proper time for insecticide application can be more accurately determined.

An efficient plan to control stink bug infestation in cotton fields needs to meet certain criteria for it to be considered successful and economically viable. The first criterion considers sampling. Due to the large number of cotton boll pods in the agricultural fields, typically a sampling method is designed and applied where a certain number of cotton bolls are harvested and examined for external and internal wall and lint damage. The second criteria concerns damage detection. The process involves manual opening of the cotton bolls and visual inspection for any signs of mechanical abrasion or damage, namely warts and lint discoloration. This type of damage examination is inherently destructive, manually tiresome, and doesn't provide reliable results. Some improvements have been made with respect to the sampling. Rather than sampling cotton bolls, populations of stink can be sampled and inferences made. In both cases, the choice to sample stink bugs or cotton bolls, the end result hasn't removed the aspects of opening up cotton bolls manually, therefore it is of utmost importance to come up with a new way to detect stink bug damage in cotton bolls, and it has to be non-invasive, more efficient, and provide more accurate results.

Recently, new approaches to this problem have been published. The first approach uses a smelling device to sense unique chemicals emitted by stink bugs and cotton bolls [42, 43]. Preliminary results are favourable. The second approach build on results first reported earlier by our group. We reported the presence of a fluorescent emission signature on infested and non-infested cotton bolls. Chlorophyll on non-infested cotton bolls fluoresces red, but on cotton bolls subjected to stink bug infestation, the puncture marks exhibit a blue/green fluorescence. This approach allows for suspected cotton bolls to be imaged and features extracted which could provide an answer as to their infestation status. The advantages of their method lay in its non-destructive course of infestation determination.

9.2 Materials and Methods

9.2.1 Stink Bug rearing

Southern green stink bugs were reared in the laboratory on a diet of fresh green beans or okra pods following the methods of Harris and Todd [45]. Briefly, adult stink bugs captured in the field were brought into the lab and placed in 37.9 liter glass aquaria lined with paper towels. Adults oviposited on the paper towels which were transferred to ventilated petri dishes until the eggs hatched and then maintained in petri dishes or small plastic wide-mouth jars at 25.0 C and 65% relative humidity. Adults used for infesting bolls were less than two weeks old and of mixed sex.

Cotton plants were started from seed and grown in the greenhouse to produce bolls for the study. Three cotton seeds (FM 9063 B2RF) per 11.35 liter plastic pot were sewn per in Metro Mix 300 growing medium. After germination, two of the plants were culled and the remaining plant was fertilized monthly with Osmocote 14-14-14 and Micromax fertilizer (the Scotts Co. LLC, Marsville, OH). Once the plant began flowering, individual white flowers were marked daily using flagging tape and then allowed to develop normally for 10 to 14 days. When the bolls reached 10 to 14 d past anthesis, a single southern green stink bug adult was caged in a mesh bag on each boll and subtending leaf for a period of 48 h. After treatment with the stink bug, bolls were excised from the plant and shipped with overnight service to the Athens campus for imaging. At the time the bolls were cut from the plant they had an external boll diameter of 2.3 to 2.5 cm. Control bolls were treated exactly as described, except that no stink bugs were introduced into the mesh bags. A total of 136 bolls were harvested that were exposed to a stink bug, and 109 control cotton bolls were harvested.

9.2.2 Imaging Apparatus and Image Acquisition

The imaging apparatus, shown in Figure 9.2, consisted of a consumer-grade digital single lens reflex (SLR) digital camera (Konica Minolta, Dynax Maxxum 7D, Tokyo, Japan) with a Sigma 50 mm f/2.8 fixed focus lens. An emission longpass filter (490nm, Chroma Technology Corp., Brattleboro, VT) was positioned on a post in front of the camera. Two LED sources (Philips/Luxeon LXHL-LR5C) with custom LED driver provided a continuous and homogeneous excitation light at 440 ± 20nm. Additional excitation bandpass filters D450/40 (Chroma) were placed on the LEDs to reduce the spectral overlap between excitation and emission light. A rotary stage held cotton bolls during imaging, and the non-fluorescent black cardboard behind reduced background fluorescence and scattered light.

Raw camera images were acquired at an exposure time of 15s and lens aperture of

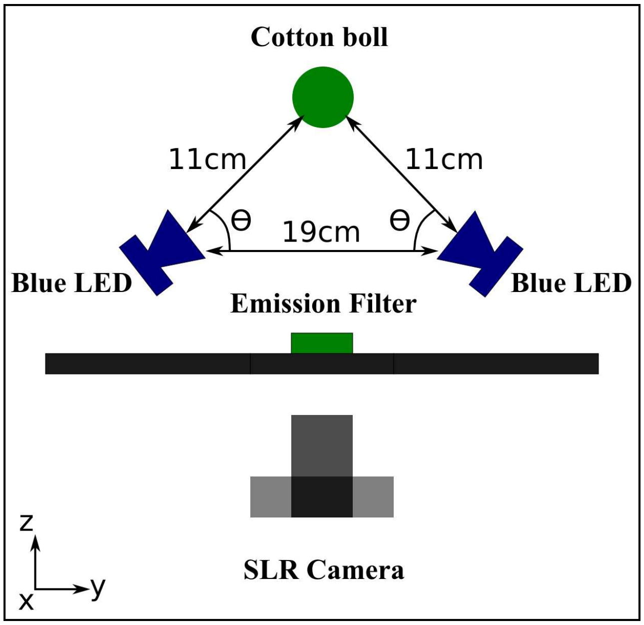

Figure 9.2: Top view of the imaging apparatus. An SLR camera was placed in front of an emission filter. Two collimated LED excitation sources positioned at angle θ=45° with respect to the cotton boll, homogeneously illuminated cotton bolls placed on a rotating pedestal.

f/11. Automatic mode was switched to manual and the camera's while balance set to 5500 K, and camera sensitivity at ISO 400. Four images were acquired per each cotton, after rotating the pedestal on which the cotton bolls sat on 90°. 12 bit/pixel Minolta raw images (MRW) were converted by zero-padding to 16 bit TIFF images with UFRaw (http://ufraw.sourceforge.net).

9.3 Image Processing and Feature Extraction

Figure 9.3 shows images of two cotton bolls: one of them is healthy, while the other one was infested with stink bugs. Chlorophyll on the healthy cotton boll fluoresces red, and on the infested cotton boll, regions where stink bugs fed on fluoresce green. To distinguish between non-infested and infested cotton bolls, an image processing and feature extraction template was applied.

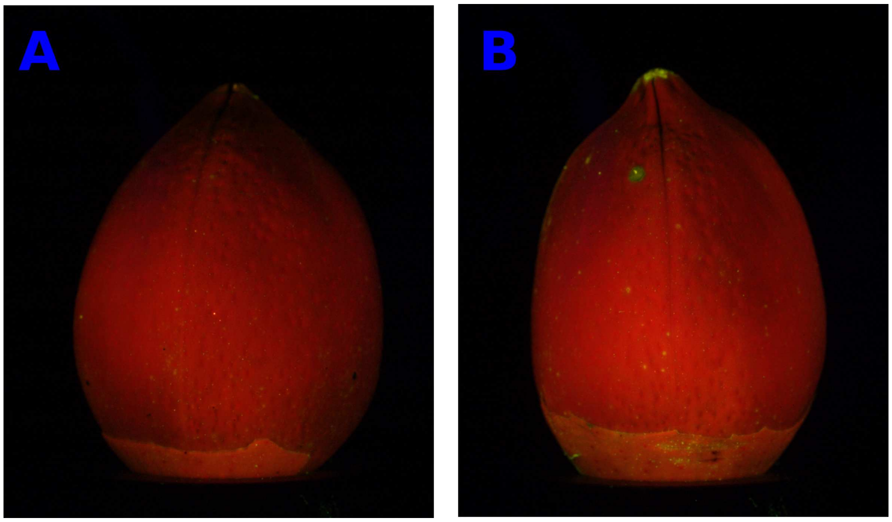

Figure 9.3: Fluorescent images of a non-infested (A) and infested (B) cotton boll. Non-infested cotton bolls shows no sings of stink bug punctures, while the infested cotton has a prominent fluorescent damaged region.

The 16 bit TIFF images were processed with CImage, an open source quantative image analysis software [46]. The schematic showing image processing steps is shown in Figure 9.4.

Images were preprocessed through noise reduction with a center-weighted median filter and binned either to 752x502 or 1504x1004 resolution (Figure 9.6). Stacked images with separate R,G,B channels were formed, while masks were created by taking the red and green channel and applying the Butterworth lowpass filter with a cutoff of 35^{-1} pixels, first valley threshold, and then binarized, so all the pixels outside of the cotton boll were set to 0, and inside the cotton boll set to 1. First valley threshold looks for the lowest intensity at which the histogram has a local minimum I_{FV}, and if its first derivative is taken, this point represents the first zero-crossing with positive slope (Figure 9.5). While it hasn't been published before, first valley threshold is implemented in CImage.

The ratiometric images were created by taking the green channel and dividing it by the

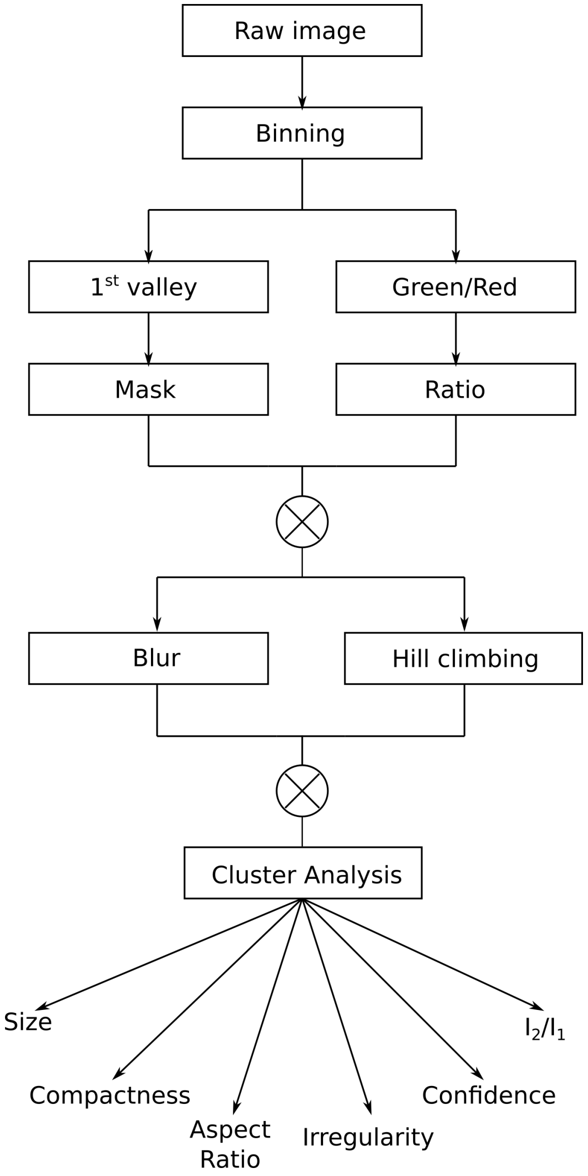

Figure 9.4: Unsupervised image analysis chain for preprocessing and feature extraction.

red channel, followed by a pixel by pixel multiplication multiplication with masks (Figure 9.7). Ratiometric images were then subjected to a smooth Gaussian blurring filter twice, and Hill-climbing algorithm apllied to locate fluorescent regions with peak intensity of 120 and maximum feature radius of 30 [47]. A cotton boll analyzer multidimensional feature vector

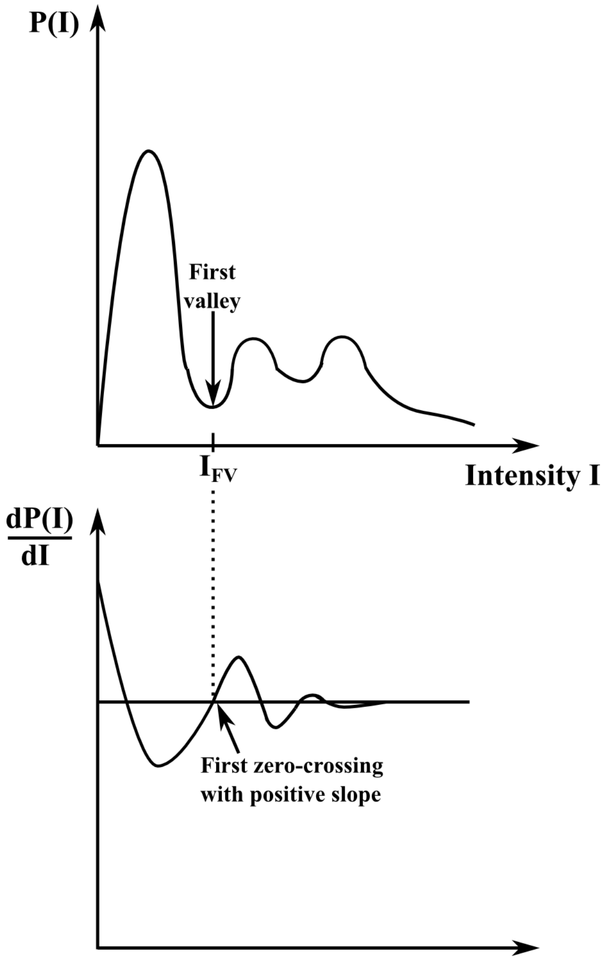

Figure 9.5: Histogram of an image describing the first valley threshold. The first valley algorithm searches for the lowest intensity at which the histogram has a local minimum (I_{FV}), which in the graph representing the first derivative of the histogram represents the first zero-crossing with positive slope.

(taking into consideration size, aspect ratio, and confidence) analyzed the regions selected by the Hill-climbing algorithm, and searched for patterns matching the puncture marks.

Size represents the number of pixels within a selected region of interest. For a selected region of interest with K boundary points, the distance of the kth boundary point at an

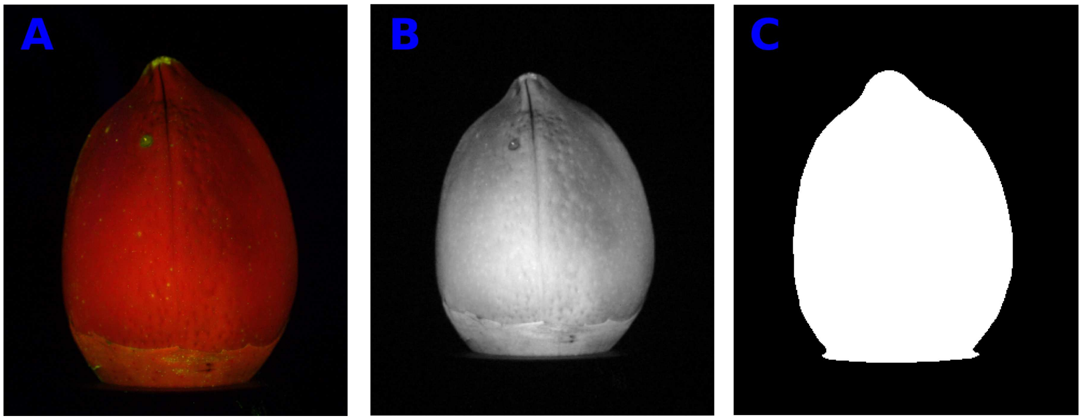

Figure 9.6: An SLR raw image (A) which is the outcome of the first multiplication in the decision tree is converted into a stack image (B), which is the outcome of the second multiplication. Green channel is then used to create a mask image (C) which has values of 1 for pixels inside the cotton boll, and values of 0 for pixels outside of the cotton boll not used in analysis. Image C is based on a low-dimensional classifier that uses the size, aspect ratio and the χ metric.

angle ϕ from the x-axis is defined as:

$$r_k = \sqrt{(x_k - x_c)^2 + (y_k - y_c)^2} \tag{9.1}$$

and angle $\phi = \frac{y_k - y_c}{x_k - x_c}$ [46]. Aspect ratio is defined as the ratio of radii of the circumscribed to the inscribed circle:

$$AR = \frac{max(r_k)}{min(r_k)} \tag{9.2}$$

Compactness of a selected region of interest is defined as:

$$C = \frac{P^2}{K} \tag{9.3}$$

where P is the number of boundary points and thus an approximation of the perimeter length. Irregularity is defined as:

$$V = \frac{\sqrt{\sum_{k=0}^{K-1} r_k^2 - \frac{1}{K}\left(\sum_{k=0}^{K-1} r_k\right)^2}}{\sum_{k=0}^{K-1} r_k} \tag{9.4}$$

where V is the coefficient of variation of r_k [46]. Confidence is defined as:

$$\chi = \frac{100\%}{1 + E^2} \tag{9.5}$$

where error E is defined as:

$$E^2 = \frac{1}{K}\sum_{A}(I(x,y) - T(x,y))^2 \tag{9.6}$$

where T(x,y) is a feature template.

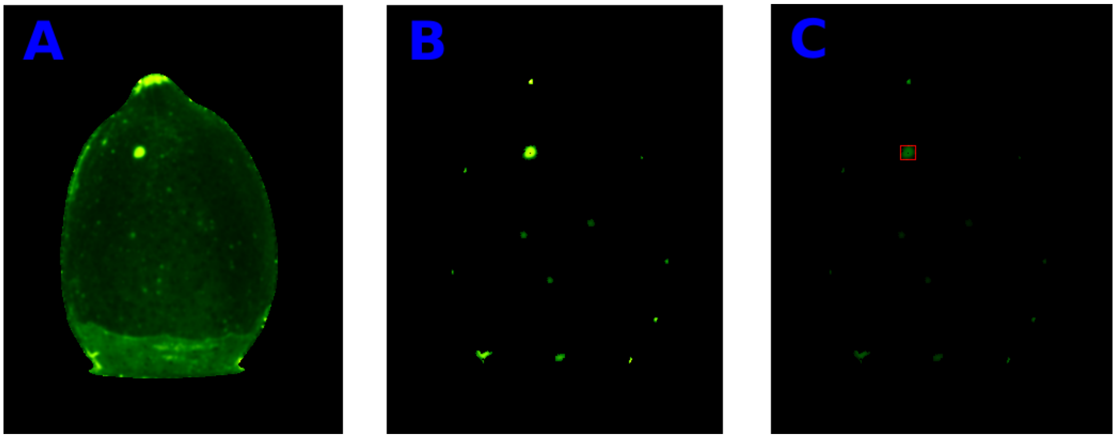

Figure 9.7: A ratiometric image (A) is created by dividing the green by the red channel and multiplying it with the mask, which sets every pixel value outside of the cotton boll to 0. Hill climbing of the ratiometric image extracts features with local maximas which are potential puncture marks. Boll analyzer selects features with patterns matching stink bug punctures (C).

9.4 Results and Discussion

Two categories of cotton bolls were analyzed: the first category contained 59 cotton bolls subjected to controlled stink bug infestation, and the second category contained 40 cotton bolls not subject to stink bug infestation. At the resolution of 754x502 pixels, out of 59 infested cotton bolls, the cotton boll analyzer found a total of 166 possible bite marks on 47 cotton bolls or 80 % of cotton bolls. For non-infested cotton bolls, the cotton boll analyzer found a total of 98 possible bite marks on 33 cotton bolls or 82.5 % of cotton bolls. The corresponding contingency table (Table 9.1) shows that sensitivity is 0.80 and specificity is 0.18.

When the resolution was doubled to 1508x1004 pixels, the cotton boll analyzer found a total of 544 possible bite marks on 59 cotton bolls or 100 % of cotton bolls. In the category of non-infested cotton bolls, a total of 526 possible bite marks were found on 38 cotton bolls or 98 % of cotton bolls. The corresponding contingency table (Table 9.2) shows that sensitivity is 1.00 and specificity is 0.05. At both resolutions, comparison between each of the classifier components (size, compactness , aspect ratio, irregularity, confidence, ratio $\frac{I1}{I2}$) is not statistically significantly different.

Table 9.1: Contigency table showing the frequency distribution of infested and non-infested cotton bolls at the resolution of 754x502 pixels, where A denotes cotton bolls with possible bite marks, and B cotton bolls without any possible bite marks. Sensitivity is 0.80, and specificity is 0.18.

	INF	NINF
A	47	33
B	12	7

Previous research demonstrated the effect of stink bug feeding on cotton bolls: the unique fluorescent signature resulting from the superficial removal of chlorophyll by the feeding mouthparts and the resulting damage to the lint rendering it commercially unviable. Subsequent research identified how by observing at the size, intensity, and ratio $\frac{I_1}{I_2}$, it is possible

Table 9.2: Contigency table showing the frequency distribution of infested and non-infested cotton bolls at the resolution of 1508x1004 pixels, where A denotes cotton bolls with possible bite marks, and B cotton bolls without any possible bite marks. Sensitivity is 1.00, and specificity is 0.05.

	INF	NINF
A	59	38
B	0	2

to narrow down further the number of possible bite marks. Here we present a cotton boll analyzer which utilizes those previous observations about stink bug damage marks and automatizes those criteria to identify possible damage. Our cotton boll analyzer uses three out of possible 6 criteria, and has the ability to look at the cotton bolls and find possible damage marks. While at this point it is not able to determine the origin of those damage, we envision a system where with the addition of artificial neural networks (ANN) or probabilistic fuzzy logic, it would be possible to create and train a system where those determinations can be made. Typically ANN examine feature vectors of much higher dimensionality, and texture metrics like Law's texture energies, statistical texture descriptors, and Haralick's texture metrics, need to be examined and included [46, 48–50].

Bibliography

[1] J.R. Lakowicz. Principles of fluorescence spectroscopy. *Journal of Biomedical Optics*, 13(2):029901–029901, 2008.

[2] T. Atsbeha, A.M. Mohammed, and M. Redi-Abshiro. Excitation wavelength dependence of dual fluorescence of dmabn in polar solvents. *Journal of fluorescence*, 20(6):1241–1248, 2010.

[3] T. Förster and G. Hoffmann. Die viskositätsabhängigkeit der fluoreszenzquantenausbeuten einiger farbstoffsysteme. *Zeitschrift für Physikalische Chemie*, 75(1_2):63–76, 1971.

[4] M.A. Haidekker, M. Nipper, A. Mustafic, D. Lichlyter, M. Dakanali, and E.A. Theodorakis. Dyes with segmental mobility: molecular rotors. *Advanced Fluorescence Reporters in Chemistry and Biology I*, pages 267–308, 2010.

[5] A. Mustafic, H.M. Huang, E.A. Theodorakis, and M.A. Haidekker. Imaging of flow patterns with fluorescent molecular rotors. *Journal of fluorescence*, 20(5):1087–1098, 2010.

[6] C. Rumble, K. Rich, G. He, and M. Maroncelli. Ccvj is not a simple rotor probe. *The Journal of Physical Chemistry A.*, 116(44):10786–10792, 2012.

[7] J. Xia, A. Mustafic, M.D. Toews, M.A. Haidekker, et al. Stink bug feeding induces fluorescence in developing cotton bolls. *Journal of biological engineering*, 5(1):11, 2011.

[8] D.R. Lide. *CRC handbook of chemistry and physics: a ready-reference book of chemical and physical data.* CRC Press, 2012.

[9] A. Tokmakoff, B. Sauter, and MD Fayer. Temperature-dependent vibrational relaxation in polyatomic liquids: Picosecond infrared pump–probe experiments. *The Journal of chemical physics*, 100:9035, 1994.

[10] J.L. Kinsey. Laser-induced fluorescence. *Annual Review of Physical Chemistry*, 28(1):349–372, 1977.

[11] T. Kübarsepp, P. Kärhä, and E. Ikonen. Interpolation of the spectral responsivity of silicon photodetectors in the near ultraviolet. *Applied Optics*, 39(1):9–15, 2000.

[12] M.A. Haidekker and E.A. Theodorakis. Environment-sensitive behavior of fluorescent molecular rotors. *Journal of biological engineering*, 4(1):1–14, 2010.

[13] E. Lippert, W. Lüder, and H. Boos. Advances in molecular spectroscopy. *Mangini, A*, 1962.

[14] Z.R. Grabowski, K. Rotkiewicz, W. Rettig, et al. Structural changes accompanying intramolecular electron transfer: focus on twisted intramolecular charge-transfer states and structures. *Chemical Reviews-Columbus*, 103(10):3899–4032, 2003.

[15] K. Rotkiewicz, K. H. Grellmann, and Z. R. Grabowski. Reinterpretation of the anomalous fluorescence of pn, n-dimethylaminobenzonitrile. *Chem. Phys. Lett*, 19:315–318, 1973.

[16] N. Mataga, Y. Kaifu, and M. Koizumi. The solvent effect on fluorescence spectrum, change of solute-solvent interaction during the lifetime of excited solute molecule. *Bulletin of the Chemical Society of Japan*, 28(9):690–691, 1955.

[17] R.O. Loutfy and B.A. Arnold. Effect of viscosity and temperature on torsional relaxation of molecular rotors. *The Journal of Physical Chemistry*, 86(21):4205–4211, 1982.

[18] M.A. Haidekker, T.P. Brady, S.H. Chalian, W. Akers, D. Lichlyter, and E.A. Theodorakis. Hydrophilic molecular rotor derivatives–synthesis and characterization. *Bioorganic chemistry*, 32(4):274–289, 2004.

[19] M.A. Haidekker and E.A. Theodorakis. Molecular rotors-fluorescent biosensors for viscosity and flow. *Org. Biomol. Chem.*, 5(11):1669–1678, 2007.

[20] M. Dakanali, T.H. Do, A. Horn, A. Chongchivivat, T. Jarusreni, D. Lichlyter, G. Guizzunti, M.A. Haidekker, and E.A. Theodorakis. Self-calibrating viscosity probes: Design and subcellular localization. *Bioorganic & Medicinal Chemistry*, 2012.

[21] H.J. Yoon, M. Dakanali, D. Lichlyter, W.M. Chang, K.A. Nguyen, M.E. Nipper, M.A. Haidekker, and E.A. Theodorakis. Synthesis and evaluation of self-calibrating ratiometric viscosity sensors. *Org. Biomol. Chem.*, 2011.

[22] M.E. Nipper, M. Dakanali, E. Theodorakis, and M.A. Haidekker. Detection of liposome membrane viscosity perturbations with ratiometric molecular rotors. *Biochimie*, 2011.

[23] J. Sutharsan, M. Dakanali, C.C. Capule, M.A. Haidekker, J. Yang, and E.A. Theodorakis. Rational design of amyloid binding agents based on the molecular rotor motif. *ChemMedChem*, 5(1):56–60, 2010.

[24] M.A. Haidekker, W. Akers, D. Lichlyter, T.P. Brady, and E.A. Theodorakis. Sensing of flow and shear stress using fluorescent molecular rotors. *Sensor Letters, 3*, 1(4):42–48, 2005.

[25] G.G. Guilbault. *Practical fluorescence*, volume 3. CRC, 1990.

[26] J. K. Greene, C. S. Bundy, P. M. Roberts, and B. R. Leonard. Identification and management of common boll feeding bugs in cotton. *Clemson Extension Report, EB158, Clemson University, Blackville, SC, USA*, 2006.

[27] A. R. Panizzi. Wild hosts of pentatomids: ecological significance and role in their pest status on crops. *Annual Review of Entomology*, 42(1):99–122, 1997.

[28] W. C. Mitchell, R. M. Warner, and E. T. Fukunaga. Southern green stink bug, nezara viridula (l.), injury to macadamia nut. 1965.

[29] J.E. McPherson and R.M. McPherson. *Stink bugs of economic importance in America north of Mexico.* CRC, 2000.

[30] P. L. Bommireddy, B. R. Leonard, and J. H. Temple. Influence of nezara viridula feeding on cotton yield, fiber quality, and seed germination. *Journal of economic entomology*, 100(5):1560–1568, 2007.

[31] E.G. Medrano, J.F. Esquivel, and A.A. Bell. Transmission of cotton seed and boll rotting bacteria by the southern green stink bug (nezara viridula l.). *Journal of applied microbiology*, 103(2):436–444, 2007.

[32] E. G. Medrano, J. F. Esquivel, R. L. Nichols, and A. A. Bell. Temporal analysis of cotton boll symptoms resulting from southern green stink bug feeding and transmission of a bacterial pathogen. *Journal of economic entomology*, 102(1):36–42, 2009.

[33] N.C. Toscano and V.M. Stern. Cotton yield and quality loss caused by various levels of stink bug infestations. *Journal of Economic Entomology*, 69(1):53–56, 1976.

[34] K.S. Barbour, JR Bradley, R. Julius, and J.S. BACHELER. Reduction in yield and quality of cotton damaged by green stink bug (hemiptera: Pentatomidae). *Journal of economic entomology*, 83(3):842–845, 1990.

[35] JK Greene, SG Turnipseed, MJ Sullivan, and GA Herzog. Boll damage by southern green stink bug (hemiptera: Pentatomidae) and tarnished plant bug (hemiptera: Miridae) caged on transgenic bacillus thuringiensis cotton. *Journal of economic entomology*, 92(4):941–944, 1999.

[36] M. M. Willrich, B. R. Leonard, and J. Temple. Injury to preflowering and flowering cotton by brown stink bug and southern green stink bug. *Journal of economic entomology*, 97(3):924–933, 2004.

[37] G. Tillman, H. Schomberg, S. Phatak, B. Mullinix, S. Lachnicht, P. Timper, and D. Olson. Influence of cover crops on insect pests and predators in conservation tillage cotton. *Journal of economic entomology*, 97(4):1217–1232, 2004.

[38] D.W. Onstad. Calculation of economic-injury levels and economic thresholds for pest management. *Journal of economic entomology*, 80(2):297–303, 1987.

[39] H. Chi. Timing of control based on the stage structure of pest populations: a simulation approach. *Journal of economic entomology*, 83(4):1143–1150, 1990.

[40] M. Toews, J. Greene, F. Reay-Jones, R. Reeves, S. Boyd, M. Huffman, D. Richter, and B. Robertson. A comparison of sampling techniques for stink bugs in cotton. In *Proceedings of the Beltwide Cotton Conferences*, pages 1193–1203, 2008.

[41] FPF Reay-Jones, MD Toews, JK Greene, and RB Reeves. Spatial dynamics of stink bugs (hemiptera: Pentatomidae) and associated boll injury in southeastern cotton fields. *Environmental Entomology*, 39(3):956–969, 2010.

[42] W. G. Henderson, A. Khalilian, Y. J. Han, J. K. Greene, and D. C. Degenhardt. Detecting stink bugs/damage in cotton utilizing a portable electronic nose. *Computers and Electronics in Agriculture*, 70(1):157–162, 2010.

[43] D. C. Degenhardt, J. K. Greene, and A. Khalilian. Temporal dynamics and electronic nose detection of stink bug-induced volatile emissions from cotton bolls. *Psyche: A Journal of Entomology*, 2012, 2012.

[44] P. Westcott. *USDA Agricultural Projections to 2019*. DIANE Publishing, 2010.

[45] VE Harris, JW Todd, et al. Comparative fecundity, egg fertility and hatch among wild-type and three laboratory-reared generations of the southern green stink bug, nezara viridula (l.)(hemiptera: Pentatomidae). *Journal of the Georgia Entomological Society*, 15(3):245–252, 1980.

[46] M. Haidekker. *Advanced biomedical image analysis*. Wiley, 2011.

[47] I.N. Bankman, T. Nizialek, I. Simon, O.B. Gatewood, I.N. Weinberg, and W.R. Brody. Segmentation algorithms for detecting microcalcifications in mammograms. *Information Technology in Biomedicine, IEEE Transactions on*, 1(2):141–149, 1997.

[48] K.I. Laws. Texture energy measures. *Proc DARPA Image Undert Workshop*, pages 47–51, 1979.

[49] R.M. Haralick, K. Shanmugam, and I.H. Dinstein. Textural features for image classification. *Systems, Man and Cybernetics, IEEE Transactions on*, (6):610–621, 1973.

[50] R.M. Haralick. Statistical and structural approaches to texture. *Proceedings of the IEEE*, 67(5):786–804, 1979.